Aerosol radiative effects and feedbacks on boundary layer meteorology and PM$_{2.5}$ chemical components during winter haze events over the Beijing-Tianjin-Hebei region

Jiawei Li[1], Zhiwei Han[*1,2], Yunfei Wu[1], Zhe Xiong[1], Xiangao Xia[3], Jie Li[1,2], Lin Liang[1,2], Renjian Zhang[1]

[1] Key Laboratory of Regional Climate-Environment for Temperate East Asia, Institute of Atmospheric Physics, Chinese Academy of Sciences, Beijing 100029, China
[2] University of Chinese Academy of Sciences, Beijing 100049, China
[3] Key Laboratory of Middle Atmosphere and Global Environment Observation, Institute of Atmospheric Physics, Chinese Academy of Sciences, Beijing100029, China
Correspondence to: Zhiwei Han (hzw@mail.iap.ac.cn)

Abstract

An online-coupled regional chemistry/aerosol-climate model (RIEMS-Chem) was developed and utilized to investigate the mechanisms of haze formation and evolution and aerosol radiative feedback during winter haze episodes in February-March 2014 over the Beijing-Tianjin-Hebei (BTH) region in China. Model comparison against a variety of observations demonstrated a good ability of RIEMS-Chem in reproducing meteorological variables, PBL heights, PM$_{2.5}$ and its chemical components, as well as aerosol optical properties. The model performances were remarkably improved for both meteorology and chemistry by taking aerosol radiative feedback into account. The domain average aerosol radiative effects (AREs) were estimated to be -57 W m^{-2} at the surface, 25 W m^{-2} in the atmosphere and -32 W m^{-2} at the top of atmosphere (TOA), respectively, during a severe haze episode (20–26 February), with the maximum hourly surface ARE reaching -384 W m^{-2} in southern Hebei province. The average feedback-induced changes in 2-m air temperature (T2), 10-m wind speed (WS10), 2-m relative humidity (RH2) and planetary boundary layer (PBL) height over the BTH region during the haze episode were -1.8 °C, -0.5 m s^{-1}, 10.0% and -184

m, respectively. The BTH average changes in PM$_{2.5}$ concentration due to the feedback were estimated to be 20.0 μg m^{-3} (29%) and 45.1 μg m^{-3} (39%) for the entire period and the severe haze episode, respectively, which demonstrated a significant impact of aerosol radiative feedback on haze formation. The relative changes in secondary aerosols were larger than those in primary aerosols due to enhanced chemical reactions by aerosol feedback. The feedback-induced absolute change in PM$_{2.5}$ concentrations was largest in haze persistence stage, followed by those in growth stage and dissipating stage. Process analyses on haze events in Beijing revealed that local emission, chemical reaction and regional transport mainly contributed to haze formation in the growth stage, whereas vertical processes (diffusion, advection and dry deposition) were major processes for PM$_{2.5}$ removals. Chemical processes and local emissions dominated the increase in PM$_{2.5}$ concentrations during the severe haze episode, whereas horizontal advection contributed to the PM$_{2.5}$ increase with a similar magnitude to local emissions and chemical processes during a moderate haze episode on 1–4 March. The contributions from physical and chemical processes to the feedback-induced changes in PM$_{2.5}$ and its major components were explored and quantified through process analyses. For the severe haze episode, the increase in the change rate of PM$_{2.5}$ (9.5 μg m^{-3} h^{-1}) induced by the feedback in the growth stage was attributed to the larger contribution from chemical processes (7.3 μg m^{-3} h^{-1}) than that from physical processes (2.2 μg m^{-3} h^{-1}), whereas, during the moderate haze episode, the increase in the PM$_{2.5}$ change rate (2.4 μg m^{-3} h^{-1}) in the growth stage was contributed more significantly by physical processes (1.4 μg m^{-3} h^{-1}) than by chemical processes (1.0 μg m^{-3} h^{-1}). In general, the aerosol-radiation feedback increased the accumulation rate of aerosols in the growth stage through weakening vertical diffusion, promoting chemical reactions, and/or enhancing horizontal advection. It enhanced the removal rate through increasing vertical diffusion and vertical advection in the dissipation stage, and had little effect on the change rate of PM$_{2.5}$ in the persistence stage.

1 Introduction

Aerosols affect radiation transfer by scattering or absorbing solar and infrared radiation, by acting as cloud condensation nuclei (CCN) to modify cloud properties, and by heating the

60 atmosphere to alter cloud formation, termed as the aerosol direct radiative effect, indirect

61 effect, and semi-direct effect (Twomey, 1974; Albrecht, 1989; Ramanathan et al., 2001),

62 respectively. In addition, there exists a set of interactions between chemistry, radiation and

63 meteorology (Dawson et al., 2007; Zhang, 2008; Isaksen et al., 2009; Baklanov et al., 2014;

64 Cai et al., 2017), which is highly complex and nonlinear and is currently one of the least

65 understood mechanisms in atmospheric science community. The above interactions are

66 traditionally not included or simplified in meteorological or chemical models, but have now

67 been considered and treated with different degrees of complexity in a few online coupled

68 models along with the advances in our knowledge and computer power, and the coupling of

69 meteorology and chemistry and its feedbacks remains one of the most challenging issues in

70 air quality and climate change (Zhang, 2008; Baklanov et al., 2014).

71 Rapid and continuous growth of economy and energy consumption in the past decades

72 has greatly elevated aerosol levels in China (Chan and Yao, 2008; Zhang et al., 2012; Li et al.,

73 2017a), resulting in serious air pollution problem and potentially significant influence on

74 radiation and climate at multi-scales. Although emission control strategies have been

75 gradually implemented in recent years, haze events still often occur in east China, especially

76 in the BTH region in wintertime due to both higher anthropogenic emissions and poorer

77 meteorological conditions. The haze issue has attracted wide attentions from public,

78 government and scientific community in China and a lot of monitoring and modeling studies

79 have been carried out to explore the sources, characteristics, formation and evolution

80 mechanisms of haze events at both urban and regional scales (Chan and Yao, 2008; Zhang et

81 al., 2012; Che et al., 2014; Guo et al., 2014; Huang et al., 2014; Sun et al., 2014; Zheng et al.,

82 2015; Cheng et al., 2016; Ding et al., 2016; Li and Han, 2016a; Cai et al., 2017; Fu and Chen,

83 2017; Li et al., 2017b; Wang et al., 2017; Huang et al., 2018; Zhang et al., 2018a; Zhong et al.,

84 2018a; Zhong et al., 2018b; An et al., 2019; Li et al., 2019a), through which our

85 understanding on haze issue has been promoted. However, there is still a large gap in our

86 knowledge about haze formation mechanism, in particular the role of

87 aerosol-radiation-meteorology feedback in haze formation and evolution (Fu and Chen, 2017;

88 Zhong et al., 2018a; An et al., 2019).

89 The aerosol radiative feedbacks on air quality and meteorology have ever been studied in

American and Europe with regional online coupled meteorology-chemistry models, such as WRF-Chem (Zhang et al., 2010; Forkel et al., 2012), which demonstrates an important role of the feedback in both air quality and meteorology. Carslaw et al. (2010) also pointed out the complexity and significance of natural aerosol interactions and feedbacks within the Earth system.

In east Asia, Han et al. (2013) revealed a significant feedback of mineral dust on dust deflation and transport, atmospheric dynamics, cloud and precipitation in spring and an improvement of model prediction for PM concentration and surface meteorology by the inclusion of the feedback effect into an online coupled chemistry-aerosol-climate model. In recent years, given the increasing concerns on severe PM pollution during haze days, some modeling studies have been conducted to investigate the effect of aerosol radiative feedback on meteorology and near surface $PM_{2.5}$ concentration, with focus on winter haze events in north China (Wang et al., 2014a; Wang et al., 2014b; Zhang et al., 2015; Gao et al., 2015; Gao et al., 2016; Qiu et al., 2017; Zhao et al., 2017; Zhang et al., 2018b; Chen et al., 2019; Wu et al., 2019). Most of the model results exhibited a positive feedback which tended to increase $PM_{2.5}$ level, but the magnitude of such feedback differs largely, with the mean fractional change in $PM_{2.5}$ concentration varying from just a few percentage (Kajino et al., 2017; Wu et al., 2019) to around 30% (Wang et al., 2014a). Some studies even show a negative feedback on $PM_{2.5}$ in Beijing (Zhang et al., 2015; Gao et al., 2016). Recently, Gao et al. (2020) reported that the aerosol–radiation feedback-induced daytime changes in $PM_{2.5}$ concentrations were less than 6% during haze days in the BTH region in January 2010 from six applications of different online coupled meteorology-chemistry models under the international framework of the MICS-Asia (Model Inter Comparison Study for Asia) Phase III. There existed some differences in the above modeling studies in terms of study period and haze level, although they were all for winter haze events in the BTH region. Zhong et al. (2018a) reported that over 70% of $PM_{2.5}$ increase during cumulative explosive stage of haze event in Beijing in winter can be attributed to the feedback effect based on integrated analysis of observations. The above studies highlight the importance and large uncertainties in the aerosol radiative feedback, which require further model development and investigation.

The diversity in the feedback effect among models could be associated with the

differences in the predictions of aerosol chemical components and aerosol optical properties, the assumption of mixing state and hygroscopic growth scheme, as well as meteorological fields, all of which determine the direction and magnitude of the feedback effect. Majority of previous model studies underpredicted PM concentrations in the north China Plain, especially for aerosol components, such as sulfate, nitrate and SOA concentrations, mainly due to incomplete understanding and unrealistic treatment of secondary aerosol formation through multi-phase chemical processes. Gao et al., (2018) reported that most of the participating models (including WRF-Chem) in the MICS-Asia (Model Inter Comparison Study for Asia) project underpredicted inorganic and organic aerosol concentrations by up to a factor of three. Besides aerosol mass concentration, the unrealistic representation of aerosol properties, such as composition, size distribution, mixing state, hygroscopic growth would also lead to model biases in aerosol optical properties and direct radiative effects. The low biases in the predicted aerosol compositions may lead to underpredictions of aerosol optical depth (AOD) and consequently of aerosol radiative effects and feedback. Che et al. (2014) reported a reduction of solar radiation by aerosols exceeding 200 W m^{-2} during a severe haze event in the north China Plain, much stronger than the estimations from models (around -100 W m^{-2}). Therefore, a realistic treatment and an accurate representation of aerosol processes and properties are crucial to the estimation of aerosol radiative effects and feedback.

It has been well recognized that high aerosol loadings can apparently reduce incoming solar radiation at the surface, leading to surface cooling and inversion associated with reduced wind speed and vertical diffusivity, and consequently increase in surface aerosol concentrations. However, while we have gained considerable knowledge on the overall feedback effect of aerosols, the detailed processes involved in the feedback mechanism are still poorly understood and barely quantified, for example, how does the aerosol radiative effect modify meteorological variables? how do the radiative and meteorological changes affect physical and chemical processes and in turn affect the magnitude and distribution of aerosol components? how to quantify the relative contributions from various physical and chemical processes to the feedback effect?

In this study, an online coupled regional climate-chemistry-aerosol model (RIEMS-Chem) was developed and applied to explore the formation and evolution of haze events during

150 February-March 2014, in which a week-long haze episode with the daily maximum PM$_{2.5}$

151 concentration up to 400 μg m^{-3} (hourly mean up to 483 μg m^{-3}) was observed. A wide variety

152 of field measurements of aerosol chemical components, optical properties, as well as

153 meteorological variables were conducted and applied to develop, constrain and validate the

154 model. The mechanisms of haze formation and evolution, aerosol radiative effects and

155 feedback on meteorology and chemistry were investigated and assessed. The overall aerosol

156 feedback on PM$_{2.5}$ and its aerosol compositions and the individual contributions to the

157 feedback from physical and chemical processes (advection, diffusion, deposition, chemistry,

158 etc.) during haze events were interpreted and quantified by a process analysis approach

159 incorporated in the model. The results from this study are expected to provide new insights

160 into the mechanism of aerosol-radiation-meteorology feedback, which is currently the source

161 of one of the largest uncertainties in haze formation and evolution.

162

163 **2 Model and Data**

164 2.1 Model description

165 An online-coupled regional atmospheric chemistry/aerosol-climate model RIEMS-Chem

166 was used in this study, which was developed based on the Regional Integrated Environmental

167 Model System (RIEMS) (Fu et al., 2005; Wang et al., 2015). A series of modules and

168 parameterizations were adopted to represent major physical processes, including a modified

169 Biosphere-Atmosphere Transfer Scheme (BATS; Dickinson et al., 1993) to simulate land

170 surface process, the Medium-Range Forecasts scheme (MRF) to represent the planetary

171 boundary layer process (Hong and Pan, 1996), the cumulus convective parameterization

172 scheme from Grell (1993), and a modified radiation package of the NCAR Community

173 Climate Model, version CCM3 (Kiehl et al., 1996) to represent radiation transfer process

174 including aerosol effect. RIEMS had been applied to investigate East Asian monsoon climate

175 and the interactions among physical, biological and chemical processes (Xiong et al., 2009;

176 Zhao, 2013; Wang et al., 2015). RIEMS had participated in the Regional Climate Model

177 Intercomparison Project (RMIP) for Asia and it was one of the best models in predicting air

178 temperature and precipitation over east Asia (Fu et al., 2005).

179   The online-coupled model RIEMS-Chem has been developed in recent years by

180   incorporating major atmospheric chemistry/aerosol processes into the host model. Pollutants

181   are driven by meteorological fields provided by RIEMS and feedback to the existing dynamic

182   and physical modules (Han, 2010; Han et al., 2012). Major atmospheric processes including

183   emission, advection, diffusion, multi-phase chemistries, dry deposition and wet scavenging of

184   pollutants are considered. The advection and diffusion for pollutants are treated with the same

185   scheme for substances (such as moisture). Gas phase chemistry is represented by an updated

186   Carbon-bond mechanism (CB-IV; Gery et al., 1989). The aerosol effect on photolysis rate is

187   considered by using the Tropospheric Ultraviolet-Visible (TUV) radiation model (Lee-Taylor

188   and Madronich, 2007). Thermodynamic processes are calculated by the ISORROPIA II

189   model (Fountoukis and Nenes, 2007). Dry deposition velocity of aerosol is calculated by a

190   size-dependent scheme which is expressed as the inverse of the sum of resistance plus a

191   gravitational settling term, while below-cloud wet scavenging of aerosol is parameterized as a

192   function of precipitation rate and collision efficiency of particle by hydrometeor (Han et al.,

193   2004). Heterogeneous reactions between gases and mineral dust and sea salt aerosols have

194   also been incorporated into RIEMS-Chem (Li and Han, 2010; Li et al., 2018a). SOA

195   formation is parameterized by a two-product model (Odum et al., 1997).

196   Current atmospheric chemistry models generally tend to underpredict sulfate

197   concentrations, especially in source regions during wintertime, such as north China, which

198   could be due to uncertainties in the treatment of chemical formation mechanism. Recent

199   model studies suggested that heterogeneous reactions could be an important pathway in

200   sulfate formation during winter haze episodes in north China (Li et al., 2017c; Li et al.,

201   2018b). Therefore, heterogeneous reactions concerning the conversion of SO_2 to sulfate on

202   pre-existed hydrated aerosols were incorporated in RIEMS-Chem. The method of Li et al.

203   (2018b) was adopted, in which the uptake coefficient (γ_{so2}) was a stepwise function

204   determined by the aerosol water content (awc) which was predicted by the ISORROPIA II

205   model. Accordingly, the upper bound of awc was set to 300 μg m^{-3} (γ_{so2}=1×10^{-4}) while the

206   lower bound was 30 μg m^{-3} (γ_{so2}=1×10^{-6}). γ_{so2} was linearly interpolated between the upper

207   and lower bounds in terms of awc.

208   RIEMS-Chem treats 9 aerosol types including sulfate, nitrate, ammonium, black carbon

209 (BC), primary organic aerosol (POA), secondary organic aerosol (SOA), anthropogenic

210 primary PMs ($PM_{2.5}$ and PM_{10}), dust and sea salt. The size distribution of the different types

211 of aerosols is previously prescribed based on the OPAC database (Optical Properties of

212 Aerosols and Clouds) (Hess et al., 1998). In this study, measurements in Beijing are used to

213 represent aerosol size distribution more realistically and to constrain the model. During the

214 study period, a scanning mobility particle sizer (SMPS; TSI, Inc., Shoreview, MN, USA) was

215 used to measure aerosol size distribution (Ma et al., 2017) and the geometric mean radius of

216 inorganic, black carbon and organic carbon aerosols were estimated to be 0.1 μm, 0.05 μm

217 and 0.1 μm, with standard deviations of 1.65, 1.6, 1.65, respectively. The above aerosol size

218 information was incorporated into RIEMS-Chem. The deflation of mineral dust is represented

219 by the scheme of Han et al. (2004) with 5 size bins (0.1–1.0, 1.0–2.0, 2.0–4.0, 4.0–8.0, 8.0–

220 20.0 μm). Primary PMs from anthropogenic are also assigned to the 5 size bins.

221   Recent observational analyses of aerosol mixing state in Beijing (Ma et al., 2012; Wu et

222 al., 2016) indicated that more than 80% aerosols were internally mixed with BC during haze

223 days, whereas about 70% of aerosols were externally mixed with BC in clean days, so an

224 internal mixing assumption was adopted for model simulation because this study focuses on

225 haze events. Recent measurements also exhibited that the geometric mean radius of aerosol

226 internal mixture during haze evolution from light-moderate to severe pollution stages just

227 increased slightly from 0.10 μm to 0.12 μm (Ma et al., 2017), so an average of 0.11 μm is

228 chosen for the geometric mean radius of internal mixture, with standard deviation of 1.65.

229   Aerosol optical parameters including extinction coefficient, single scattering albedo and

230 asymmetry factor were calculated by a Mie-theory based method developed by Ghan and

231 Zaveri (2007). In this method, the optical properties of different types of aerosols are

232 pre-calculated by Mie theory and fitted by Chebyshev polynomials, which are functions of

233 aerosol geometric mean diameter and refractive index:

234
$$Q = \exp\left[\sum_{k=1}^{10} A_k T_k(x)\right], \tag{1}$$

235
$$x = \frac{2\log(D_p) - \log(D_{min}) - \log(D_{max})}{\log(D_{max}) - \log(D_{min})}, \tag{2}$$

236 where Q represents the aerosol optical properties (such as scattering efficiency). $T_k(x)$ are the

Chebyshev polynomial of order k, which is related to particle size, A_k are the Chebyshev coefficients which is related to refractive index, D_p is the geometric mean diameter, D_{min} and D_{max} are the minimum and maximum D_p for obtaining the Chebyshev polynomials, with values of 0.001 μm and 10 μm, respectively. It has been proved that 40 groups of D_p in the range from D_{min} and D_{max} are sufficient to control errors below 10% compared with classical Mie code calculation.

The effect of water uptake is treated by the κ-Köhler parameterization (Petters and Kreidenweis, 2007), which calculates aerosol wet diameter due to hygroscopic growth under different relative humidity. The bulk κ for internal mixture of aerosols is derived by the volume-weighted average of κ of each aerosol component, while the κ values for inorganic aerosols, BC, POA, SOA, dust and sea salt were set to 0.65, 0, 0.1, 0.2, 0.01 and 0.98, respectively, according to previous observational and modeling studies (Riemer et al., 2010; Liu et al., 2010a; Westervelt et al., 2012):

$$\kappa = \sum_j \frac{V_j}{V_a} \kappa_j, \tag{3}$$

where V_a is the total volume of dry aerosols, V_j is the volume of each aerosol component j.

The refractive index of internally mixed aerosols is calculated using the Maxwell-Garnett mixing rule:

$$R_w^2 = R_s^2 \left[\frac{R_i^2 + 2R_s^2 + 2f_i(R_i^2 - R_s^2)}{R_i^2 + 2R_s^2 - f_i(R_i^2 - R_s^2)} \right], \tag{4}$$

$$f_i = \frac{V_i}{V}, \tag{5}$$

where R_w is the refractive index of the internal mixture, R_i and R_s are the refractive index of insoluble components (BC and POA) and soluble components (inorganic aerosols, SOA and water), respectively. V_i represents the volume of insoluble components, V represents the total volume of wetted aerosols.

After obtaining the wet diameter (D_p) and refractive index of the internally mixed aerosols (R_w), the aerosol optical properties (Q) can be derived from formula (1) with the Chebyshev fitting coefficients table. Then, aerosol optical parameters, such as extinction coefficient can be obtained through multiplying Q by aerosol mass concentration from

264 chemical module. The advantage of this optical module is the computational speed is much

265 faster than that from the traditional Mie calculation, with a similar level of accuracy. This

266 module has been successfully used in estimations of aerosol optical properties and direct

267 radiative effects over East Asia (Han et al., 2011a; Li and Han, 2016b; Li et al., 2019b).

268 An empirical method from Hegg (1994) is applied to link cloud droplet number

269 concentration N_c to mass concentration of hydrophilic aerosols (sulfate, nitrate, hydrophilic

270 BC and OC) to represent the first indirect effect, while the parameterization of Beheng (1994)

271 is used to represent the second indirect effect, in which the autoconversion rate converting

272 from cloud water to rain water depends on N_c and cloud liquid water content W_L. The cloud

273 effective radius r_e is calculated based on N_c, W_L and the cube of the ratio of the mean volume

274 radius and the effective radius of the cloud-droplet spectrum following Martin et al. (1994).

275 The effect of aerosols on ice nuclei and convective cloud is not treated yet in this model

276 because of the complexity and limitation in knowledge.

277 The aerosol optical parameters and N_c due to aerosol activation calculated above are

278 transferred into radiation module to account for the perturbation of radiation and atmospheric

279 heating rate due to aerosol direct and indirect effects. The following land surface module and

280 boundary layer module account for the changes in land-air fluxes of heat and moisture,

281 turbulent diffusion coefficients and meteorological variables in the boundary layer in

282 response to the radiation change, and then air temperature tendency is calculated in terms of

283 the altered atmospheric heating rate and radiation, which further lead to changes in

284 meteorological variables, and in turn affect physical and chemical processes and

285 concentrations of aerosols and their precursors represented in the chemical module. All the

286 modules are called every 2.5 minutes and the transfer of variables between chemical module

287 and radiation/meteorological modules is made every 30 minutes.

288 RIEMS-Chem has been successfully applied in previous modeling studies of

289 anthropogenic aerosols, mineral dust and marine aerosols regarding spatial-temporal

290 distributions, physical and chemical evolutions, radiative and climatic effects over east Asia

291 (Han et al., 2011b; 2012; 2013; 2019; Li et al., 2014; Li and Han, 2016b; 2016c; Li et al.,

292 2019b). RIEMS-Chem have been participating in the international model comparison project

293 Model Inter Comparison Study for Asia phase III (MICS-Asia III) and shows a good ability

294   in predicting PM$_{2.5}$ concentration and AOD over East Asia (Gao et al., 2018).

295

296   2.2 Process analysis

297   In RIEMS-Chem, a time-splitting scheme based on continuity equation is applied to

298   predict species concentrations; therefore, the species concentrations are the net results of

299   successive changes in concentration due to different atmospheric physical and chemical

300   processes, and the changes in species concentration by each process can be recorded,

301   allowing the quantification of individual contribution of each process to species variation. In

302   this study, a process analysis (PA) scheme, which calculates the Integrated Process Rates

303   (IPR) at each time step and each grid, was embedded in RIEMS-Chem to identify the

304   contributions of physical and chemical processes to aerosol evolution. At each time step, the

305   IPR for a certain process was calculated by subtracting the species concentrations at the

306   beginning of this process from the ones after the process. The IPR method has ever been

307   applied to study the formation and fate of particulate and gaseous pollutants in North America

308   and China (e.g. Yu et al., 2008; Zhang et al., 2009; Liu et al., 2010b). The processes involved

309   in aerosol evolution include emissions of primary species, advections (horizontal and

310   vertical), diffusions (horizontal and vertical), dry deposition, chemical processes (gas-phase

311   chemistry, thermodynamic equilibrium and heterogeneous reactions), cloud processes and

312   wet deposition. Here cloud process represents the effects of cloud attenuation of photolysis

313   rate, aqueous-phase chemistry and in-cloud mixing. In this study, PA is applied not only to

314   quantify the contributions of individual physical and chemical processes to haze evolution,

315   but also to help interpret the processes involved in aerosol radiative feedback. In addition,

316   different from the previous PA application, chemical processes are further classified into gas

317   phase, thermodynamic and heterogeneous reactions to provide more details on chemical

318   pathways of secondary aerosol formation. The mass balance of IPR has been examined,

319   assuring that the change in species concentration during one time step is equal to the sum of

320   IPRs by each of the processes.

321

322   2.3 Emission inventories

323   Monthly mean anthropogenic emissions of sulfur dioxide (SO$_2$), nitrogen (NO$_x$),

324   ammonia (NH_3), non-methane volatile organic compounds (NMVOC), carbon monoxide

325   (CO), black carbon (BC), primary organic carbon (POA), other anthropogenic primary $PM_{2.5}$

326   and primary PM_{10} in China for the year 2014 were obtained from the MEIC inventory

327   (Multi-resolution Emission Inventory for China) which was developed by Tsinghua

328   University (http://meicmodel.org). Anthropogenic emissions outside China were taken from

329   the MIX inventory which was developed to support the Model Inter-Comparison Study for

330   Asia phase III (MICS-Asia III) and the Hemispheric Transport of Air Pollution (HTAP)

331   projects (Li et al., 2017a). Both inventories of MEIC and MIX have the horizontal resolution

332   of 0.25 degree. Biomass burning emissions of aerosols and gas precursors for the year 2014

333   with a horizontal resolution of 0.25 degree were derived from the fourth version of the Global

334   Fire Emissions Database (GFED4) (Giglio et al., 2013). Monthly mean biogenic emissions of

335   isoprene and monoterpene were derived from Global Emissions Inventory Activity (GEIA,

336   http://www.geiacenter.org/). The above emission data were bilinearly interpolated to the

337   lambert projection of RIEMS-Chem.

338

339   2.4 Model configuration and numerical experiments

340   RIEMS-Chem was configured on a lambert conformal projection with horizontal

341   resolution of 60 km, covering most areas of China, the Korean Peninsula, Japan and part of

342   the Indo-China Peninsula (Figure 1). 16 vertical layers distributed vertically and unevenly in

343   the terrain-following sigma coordinate, with the lowest 8 layers within the boundary layer.

344   This study focused on the Beijing-Tianjin-Hebei (BTH) region with more attentions to the

345   Beijing metropolitan. The study period was from 10 February to 12 March, 2014,

346   encountering several haze episodes. The first 7 days were taken as model spin-up and the

347   results from 17 February to 12 March were used for analysis.

348   Initial and boundary conditions for meteorological variables were provided by the final

349   reanalysis data (FNL) with 1°×1° resolution and 6-hourly interval from the National Centers

350   for Environmental Prediction (NOAA/NCEP, 2000). Lateral boundary conditions of chemical

351   species at 6-hourly interval were derived from the simulations of the global chemical model

352   MOZART-4 (Model for Ozone and Related chemical Tracers, version 4; Emmons et al.,

353   2010).

354   To investigate the aerosol radiative effects and its potential feedback on solar radiation,

355   meteorological variables, planetary boundary layer (PBL) and aerosol concentrations in the

356   study domain, two simulations were designed. The FULL simulation (with aerosols)

357   considered all aerosol direct and indirect effects and feedbacks, and the NoAer simulation

358   shuts off aerosol direct radiative effects and removes anthropogenic aerosols in aerosol

359   indirect effects. In both simulations, the driving meteorological data, emissions and model

360   settings were exactly the same.

361

362   2.5 Observational data

363   Several observational datasets for meteorological variables, aerosol concentrations and

364   aerosol optical parameters were obtained and used for model comparison and analysis.

365   In-situ 3-hourly observations of temperature at 2 meter (T2), wind speed at 10 meter

366   (WS10) and relative humidity at 2 meter (RH2) from three meteorological monitoring sites

367   around Beijing (Figure 1) were collected from the China Meteorological Data Service Center

368   (CMDS) (http://data.cma.cn/).

369   To evaluate the model ability in reproducing evolution of planetary boundary layer

370   (PBL), high-frequency sounding data measured around 14:00 LST at the Xianghe station

371   (39°45′N, 116°58′E; approximately 63 km southeast of Beijing downtown) were collected,

372   from which the PBL height can be determined based on the vertical gradients of virtual

373   potential temperature and water mixing ratio according to the method from Heo et al. (2003).

374   This sounding dataset provided a good indicator of mixing layer height because the sounding

375   was launched at 14:00 LST and lasts for about one hour. The meteorological sounding was

376   launched in Xianghe once a week (every Tuesday) and totally four soundings were available

377   during the study period (18 and 25 February, 4 and 11 March). Fortunately, the four

378   soundings encountered one severe haze episode, one moderate haze episode, and two clean

379   days, providing robust evidences on day-to-day variation of mixing layer height under

380   various atmospheric conditions. Hourly downward shortwave radiation flux (SWDOWN) at

381   the surface was measured simultaneously at the Xianghe station by a pyranometer with sun

382   shield and was used in this study.

383   The measurements of mass concentrations of $PM_{2.5}$ and its components and aerosol

384 optical parameters were carried out at the tower division of the Institute of Atmospheric

385 Physics (IAP), Chinese Academy of Sciences (CAS) in Beijing (39°58′N, 116°22′E) from 17

386 February to 12 March, 2014. Real-time hourly $PM_{2.5}$ mass concentrations were online

387 measured by a hybrid beta attenuation particulate monitor (Model 5030 SHARP, Thermo

388 Scientific, USA). $PM_{2.5}$ samples were collected in parallel by an R&P Partisol®Model 2025

389 dichotomous sequential PM air sampler (Thermo, USA) and a MiniVol TAS PM sampler

390 (Airmetrics, USA) between 24 February and 12 March, 2014. Samples were collected twice

391 per day with one during the daytime (from 7:00 to 19:00 LST) and the other at night (from

392 19:00 to 7:00 of the next day). Totally 33 half-day samples were collected. Aerosol chemical

393 compositions including sulfate (SO_4^{2-}), nitrate (NO_3^-), ammonium (NH_4^+), BC and OC were

394 analyzed by ion chromatography (Dionex ICS-90 for cations and ICS-1500 for anions) and a

395 DRI-2100A carbonaceous aerosol analyzer. Real-time hourly aerosol extinction coefficient

396 and aerosol absorption coefficient at dry condition (RH=10%) were synchronously measured

397 by a nephelometer (Aurora3000) and an aethalometer (AE-31), respectively. Detailed

398 information about this experiment including the sampling site, instruments, measurement

399 procedures and sample analysis were well documented in Ma et al. (2017). The mass

400 concentration of SOC was estimated using a revised EC tracer method (Zhao et al., 2013).

401 Measurements of AOD at the 4 sites (Nanjiao, Tianjin, Gucheng and Shangdianzi) in the

402 BTH region were obtained from the China Aerosol Remote Sensing Network (CARSNET)

403 (Che et al., 2014). Nanjiao is an urban site located in southern Beijing. Tianjin site is located

404 in the center of Tianjin city, about 120 km to the southeast of Beijing. Gucheng, a suburban

405 site in Hebei province, is about 130 km to the southwest of Beijing downtown. Shangdianzi is

406 located 150 km to the northeast of Beijing, which is a background station since it is far away

407 from anthropogenic sources. Daily mean AOD was derived by temporally averaging the raw

408 data measured by sunphotometer during daytime. To compare with the model output, AOD at

409 550 nm was used.

410

411 **3 Model validations**

412 3.1 Meteorological variables

413   Wind speed, temperature and relative humidity are key meteorological factors affecting

414   physical and chemical processes of atmospheric pollutants. The statistics for comparison

415   between in-situ observation and the FULL simulation for WS10, T2 and RH2 are presented in

416   Table 1. At the 3 sites (Beijing, Tianjin and Tanggu), the model performances were

417   reasonably good, although wind speeds were somewhat overpredicted. The overall

418   correlation coefficient (R) and normalized mean bias (NMB) at the 3 sites were 0.83 and -2%

419   for T2, 0.61 and -1% for RH2 and 0.47 and 31% for WS10. In all, RIEMS-Chem was able to

420   reasonably reproduce the meteorological variables during the study period. The statistics for

421   NoAer simulation are also list in Table 1. It is noteworthy that the statistics for the FULL

422   simulation are overall better than those for NoAer simulation, such as the warm bias in the

423   simulated air temperature and positive bias in wind speed are apparently reduced. This

424   demonstrates the inclusion of aerosol radiative effects does improve meteorological

425   prediction in this study.

426   The observed hourly SWDOWN in Xianghe was compared with model simulation

427   (Figure 2a). In general, the FULL case well reproduced SWDOWN in clean days and

428   light-moderate polluted days, but tended to underpredict observations in heavy haze days,

429   such as the period from 20 to 26 February. Underpredictions of cloud amount and PM

430   concentrations could be reasons for the low bias. For the entire study period, the observed

431   and simulated (FULL) mean SWDOWN were 136.0 W m^{-2} and 188.4 W m^{-2}, respectively,

432   with R of 0.91 (Figure 2a). If only days with low cloud covers were considered, the

433   SWDOWNs were 183.3 W m^{-2} and 213.7 W m^{-2} from observation and the FULL case,

434   respectively, with the NMB of 16%. In contrast, the NoAer case failed to capture the

435   decreasing tendency of SWDOWN during haze days, resulting in a larger bias (NMB of 72%)

436   than the FULL case.

437   To examine the model performance for meteorology in the vertical direction, we

438   collected meteorological sounding data at Beijing observatory from the website of University

439   of Wyoming (http://weather.uwyo.edu/upperair/sounding.html). Figure S1 and S2 present the

440   average observed and simulated vertical profiles of air temperature, wind speed and relative

441   humidity at 08:00 LST and 20:00 LST during the two haze episodes of 20-26 February and

442   1-4 March 2014 and the corresponding comparison statistics for these variables in the

443 troposphere and at altitudes below 3 km are listed in Tables S1 and S2. In general, the model

444 is able to generally capture the major features of vertical distribution of key meteorological

445 variables, although the model tends to predict higher relative humidity in the middle-upper

446 troposphere. Such overpredictions are also found for the same region in previous studies,

447 such as WRF-Chem simulation (Gao et al., 2016). The statistics indicate that the model

448 simulated vertical distribution of meteorological variables are within an acceptable accuracy

449 range of current meteorological model predictions.

450

451 3.2 Planetary boundary layer (PBL) height

452 Figure 2b shows the simulated PBL heights at 14:00 LST from the FULL case and

453 NoAer case during the study period and the observed PBL heights at 14:00 LST determined

454 from air soundings on 18 February (clean), 25 February (severe haze), 4 March (clean) and

455 11 March (haze), 2014, respectively. There was large variation in PBL height in the afternoon,

456 with higher PBL height in clean days and lower one in haze days, inversely related to the

457 $PM_{2.5}$ level. The FULL case well reproduced the very low PBL height during the most severe

458 haze episode on 25 February, with the observed and simulated PBL heights to be 569 m and

459 587 m, respectively. In clean days, the much higher mixing layer was also well captured, such

460 as, on 4 March, the observed and simulated PBL heights were 2305 m and 2535 m,

461 respectively. It is noteworthy that the simulated PBL heights in the NoAer case were

462 consistently higher than those in the FULL case, and the PBL height simulation from the

463 FULL case (considering aerosol radiative effects) was apparently in a better agreement with

464 observation than that from the NoAer case, except for that on 18 February.

465

466 3.3 Mass concentrations of $PM_{2.5}$ and aerosol components

467 Figure 2c shows the hourly $PM_{2.5}$ mass concentrations observed at the IAP site and those

468 from the FULL simulation and NoAer simulation. The study period was characterized by

469 three haze episodes, which was the episode 1 on 20–26 February, the episode 2 from 1 to 4

470 March, and the episode 3 from 8 to 11 March. The first episode experienced the most severe

471 pollution with the maximum hourly $PM_{2.5}$ concentration exceeding 480 μg m^{-3} on 25

472 February. The second and third ones were moderately polluted in terms of magnitude and

473   lasting time. In general, the model reproduced the hourly variation of PM$_{2.5}$ concentrations

474   reasonably well in the FULL case, although the peaks were somewhat underpredicted in

475   some days, which could be partly due to the overprediction of wind speed (Table 1) and

476   potential uncertainties in emission inventories. The low bias in PM$_{2.5}$ concentrations could

477   also contribute to the overprediction of SWDOWN during the first haze episode (20-26

478   February) discussed in section 3.1. The average PM$_{2.5}$ concentrations during the study period

479   were 142.0 μg m^{-3} and 131.4 μg m^{-3} from observation and the FULL simulation, respectively,

480   with R of 0.8 and NMB of -7% (Table 2), which demonstrates a good model performance for

481   PM$_{2.5}$ predictions for the winter haze periods. A remarkable feature shown in Figure 2 is the

482   significant negative correlation between PM$_{2.5}$ concentration and PBL height and SWDOWN.

483   The comparison between the simulated daily mean surface aerosol components (sulfate

484   (SO$_4^{2-}$), nitrate (NO$_3^-$), ammonium (NH$_4^+$), BC and OC) and observations at the IAP site are

485   presented in Figure 3. The daily mean observation in the figure is an average of the half-day

486   samples, while the original half-day samples are used for statistics calculation in Table 2. The

487   model (from the FULL case) generally exhibits a good performance for inorganic aerosol

488   (sulfate, nitrate and ammonium) concentrations in terms of both daily variation and

489   magnitude (Figure 3a - 3c). It is encouraging that the maximum values on 25 February during

490   the first haze episode and the moderate values on 3 March in the second haze episode are

491   well reproduced, although some low biases occurred in the last few days. On average, the

492   model simulations of 20.3 μg m^{-3}, 24.3 μg m^{-3} and 13.9 μg m^{-3} are very close to the

493   observations of 21.0 μg m^{-3}, 26.0 μg m^{-3} and 14.1 μg m^{-3} for sulfate, nitrate and ammonium,

494   respectively, with Rs of 0.92, 0.88 and 0.91 and NMBs of -4%, -6% and -2%, respectively

495   (Table 2). Most of the online coupled models tended to underpredicted sulfate concentration

496   (Gao et al., 2016; Qiu et al., 2017; Gao et al., 2018), which led to an underestimation of

497   aerosol optical depth and radiative effect. The model in this study improves the simulation of

498   inorganic aerosols, mainly through the inclusion of heterogeneous chemical reactions for

499   inorganic aerosols.

500   The model also reproduced the temporal variation and magnitude of BC (Figure 3d) and

501   OC (Figure 3e) concentrations in Beijing reasonably well. However, the model tended to

502   underpredict the peak OC values on 24–25 February and to overpredict BC concentrations

503 from late February to early March. The low bias in OC simulation during the haze episodes

504 could be attributed to the underprediction of SOC (Figure 3f) due to potentially missing

505 chemical pathways. Uncertainties in the emission inventory could also be a reason. Li et al.,

506 (2017a) reported the uncertainties in BC and OC emissions for China could be ±200%, larger

507 than those of emissions for gases (<70%) and primary PMs (~130%). The period mean BC

508 concentrations from observation and simulation were 5.2 $\mu g\ m^{-3}$ and 6.7 $\mu g\ m^{-3}$, respectively,

509 with R of 0.92 and NMB of 28% (Table 2). The period mean simulated and observed POC

510 concentrations were 18.4 $\mu g\ m^{-3}$ and 15.5 $\mu g\ m^{-3}$, respectively, with R of 0.93, whereas the

511 simulated SOC concentration was 9.9 $\mu g\ m^{-3}$, lower than observation (13.6 $\mu g\ m^{-3}$) by 27%,

512 with a correlation coefficient of 0.56. For OC (sum of POC and SOC), the simulated value

513 (28.3 $\mu g\ m^{-3}$) was very close to the observation (29.1 $\mu g\ m^{-3}$), with R of 0.88 and NMB of

514 -3%, respectively, which indicated a generally good model performance for the total OC

515 concentration.

516 It is noteworthy that by considering aerosol radiative effects, the model apparently

517 improved simulations for both $PM_{2.5}$ and its chemical compositions, which is illustrated by

518 comparing model results between the FULL and NoAer cases (Figure 2c, Figure 3 and Table

519 2). Another important finding is that the duration of haze episode was prolonged by about 2–3

520 hours by the aerosol radiative feedback compared with that without aerosol feedback (Figure

521 2c).

522 To evaluate the overall model performance on $PM_{2.5}$ and its gas precursors in the BTH

523 region, we also collected observations at 80 surface stations in 13 cities of the BTH from the

524 website of CNEMC (China National Environmental Monitoring Center)

525 (http://www.cnemc.cn/) and made a detailed comparison between observations and model

526 simulations for $PM_{2.5}$, O_3, NO_2 and SO_2. The observed and simulated hourly mass

527 concentrations of these species in some typical cities are presented in Figure S3 - S8 and the

528 statistics for each city and for all the cities are presented in Table S3. The overall model

529 ability is generally satisfactory, with Rs of 0.87, 0.81, 0.60 and 0.74, NMBs of -0.4%, -11%,

530 -17% and 0.5% for $PM_{2.5}$, O_3, SO_2 and NO_2, respectively, for all the sites in the BTH region.

531

532 3.4 Aerosol optical parameters

533   Figure 4a and 4b show the measured and simulated hourly aerosol extinction coefficient

534   (EXT) and aerosol absorption coefficient (ABS) at an RH of 10% at the IAP site during the

535   study period. It clearly showed that the model was able to well reproduce the magnitudes and

536   temporal variations of EXT and ABS under dry condition in the FULL case, although the

537   model tended to predict higher ABS in some days possibly due to the overprediction of BC

538   concentration. Single scattering albedo (SSA) which is defined as the ratio of scattering

539   coefficient (EXT minus ABS) to extinction coefficient is also given in Figure 4c. The FULL

540   case generally simulated high SSA values during haze episodes, such as 0.92 on 20–26

541   February, 0.85–0.9 from 1 to 4 March and 0.8–0.9 on 8–11 March, suggesting a dominant

542   role of light scattering aerosols in haze days. It is encouraging that the model reproduced SSA

543   during the severe haze episode (on 20–26 February) quite well, with both the simulation and

544   observation being approximately 0.92. However, SSA observation in clean days (such as on

545   5–7 March) was lower than that in haze days, and the model tended to overpredict SSA in

546   clean days, which could be attributed to uncertainties in measurement. In clean days, both the

547   denominator (EXT) and numerator (EXT minus ABS) were small, a subtle perturbation in

548   EXT and/or ABS can result in a large variation in SSA. A previous observational study in

549   Beijing suggested that SSA observation was more uncertain in clean days than in polluted

550   days because the observed aerosol extinction coefficient was too low in clean days (Jing et al.,

551   2015). On average, the observed EXT, ABS and SSA values were 0.51 km^{-1}, 0.048 km^{-1} and

552   0.85, respectively, whereas, the corresponding FULL simulations were 0.53 km^{-1}, 0.052 km^{-1}

553   and 0.88, with Rs of 0.8, 0.7 and 0.7 and NMBs of 4%, 10% and 5%, respectively (Table 2).

554   The above comparison demonstrates a good ability of the model in estimating aerosol optical

555   properties during the study period, which could be attributed to both the good performance

556   for aerosol compositions and the realistic representation of aerosol properties (aerosol size

557   distribution, mixing state, hygroscopic growth etc.), which is based on real-time

558   measurements in Beijing.

559   Besides EXT and ABS measured under dry condition, measurements of AOD at the four

560   CARSNET sites around Beijing (Nanjiao, Tianjin, Gucheng and Shangdianzi) were also used

561   to evaluate the model ability in simulating aerosol optical parameters in real atmosphere

562   (Figure 5). At the Nanjiao site, which is about 50km southeast of Beijing downtown (Figure

5a), AOD measurement was unavailable in most days during the first haze episode (20 to 26 February), with only two data (around 4.8) available on 25 February. The simulated daily AOD from the FULL case varied from 3.1 to 4.0 during 24 - 26 February, somewhat lower than the observation. The model tended to simulate lower AOD during the third haze episode (8 to 11 March), which can be partly attributed to the predicted lower aerosol concentrations. The measured AODs in Gucheng (southwest to Beijing) and Tianjin were similar in terms of variation and magnitude (Figures 5b and 5c), showing high values during pollution periods with the maximum daily AOD exceeding 4.0 in Gucheng and 3.5 in Tianjin. The FULL case reproduced the AOD variations and magnitudes reasonably well at the two sites although low biases still occurred during 8 to 11 March in Gucheng. For the regional background site Shangdianzi (Figure 5d), the magnitude and variation of AOD were similar to those in Nanjiao, suggesting that the haze episodes were regionally distributed because the temporal variations and magnitudes of AOD were generally consistent at the four sites.

Table 3 summaries the performance statistics for daily mean AOD. In general, the model reproduced the temporal variation and magnitude of AOD around Beijing reasonably well with the overall R of 0.81 (0.67–0.90) and NMB of -8.6% (-15.6%–6.2%). The underestimation is mainly contributed by the low biases during the third haze episode (8 to 11 March) when inorganic aerosol concentrations were underestimated (Figure 3a–3c). In addition, the limitation in AOD samples during the severe haze episode in Nanjiao and Shangdianzi could amplify the negative bias. At the Gucheng and Tianjin sites where more samples were available, the mean measured AODs were 1.7 and 1.4, respectively, agreeing well with the simulated values of 1.5 and 1.3 from the FULL case.

In summary, the above comparisons demonstrate that RIEMS-Chem was capable in reproducing the spatial distribution and temporal variation of meteorological variables (air temperature, wind speed, surface shortwave radiation, PBL height etc.), concentrations of total $PM_{2.5}$ mass and its chemical compositions and aerosol optical properties during the winter haze periods around Beijing. It is also noteworthy that the inclusion of aerosol radiative effects apparently improved the overall model performance for both meteorological variables and aerosol physical and chemical properties, highlighting the necessity to develop online coupled chemistry-meteorology model for both air quality and climate research. The

593 good agreement above increases confidence in the reliability of the following model results

594 on aerosol radiative effects and feedback.

595

4 Model results

597 4.1 Distributions of meteorological variables and near surface $PM_{2.5}$ concentration

598 The period-mean distributions of near-surface wind speed (WS10), temperature (T2),

599 relative humidity (RH2), PBL height and $PM_{2.5}$ concentration are shown in Figures 6a to 6e.

600 During the study period, westerly winds dominated the northwestern parts of the BTH region

601 while southeasterly prevailed over the southeastern parts, as a result, the near-surface wind

602 speeds were fairly weak over the convergence zone from southern Hebei province to Beijing

603 (Figure 6c). Such wind pattern indicated that pollutants from southern parts of the domain

604 (such as Shandong and Henan provinces) can be transported northward to Beijing, Tianjin

605 and Hebei, and air pollutants over the weak-wind regions were easily accumulated to high

606 level. Near-surface temperature showed an apparent south-to-north gradient, with surface air

607 temperature in a range of 4 °C to 6 °C over the southern BTH region, -2 °C to 2 °C in the

608 vicinity of Beijing and parts of central Hebei, and lower than -2 °C in northern parts of the

609 domain (Figure 6a). Relative humidity was higher (~65% to 75%) over northern areas and

610 lower (~55% to 65%) over southern areas (Figure 6b). PBL height also exhibited an apparent

611 gradient in spatial distribution (Figure 6d), ranging from 800-1000 m in northern Hebei and

612 Inner Mongolia to about 600-700 m in southern Beijing, Tianjin and southern Hebei. A belt of

613 high $PM_{2.5}$ concentration spread from southwest to northeast (Figure 6e), with the maximum

614 value up to 150 μg m^{-3} in the vicinity of Shijiazhuang and Beijing and Tianjin. The regions

615 with high $PM_{2.5}$ concentrations generally corresponded well to the weak-wind areas shown in

616 Figure 6c.

617 Averaged over the BTH region and the entire study period, the simulated T2, WS10, RH2,

618 PBL height and $PM_{2.5}$ concentration from the FULL case were 0.61 °C, 1.2 m s^{-1}, 67.0%,

619 698.4 m and 90.0 μg m^{-3}, respectively. According to the "Technical Regulation on Ambient

620 Air Quality Index" prescribed by Chinese Ministry of Environmental Protection in 2012, a

621 pollution event occurs when 24-hr mean $PM_{2.5}$ concentration $\geq$ 75 μg m^{-3}. Totally, there were

622   11 days with domain and daily average $PM_{2.5}$ concentration exceeding 75 μg m^{-3} in the BTH

623   region, with the maximum exceeding 136 μg m^{-3}, indicating the severity of air pollution

624   during the study period.

625

626   4.2 Distributions of AOD, SSA and aerosol direct radiative effects

627   Figure 6f shows that high AODs mainly distributed from northern Beijing to

628   southwestern Hebei, southern Shanxi and northern Henan provinces, with the maximum up to

629   1.1. As AOD was determined by vertical profiles of aerosol compositions and RH, the spatial

630   distribution of AOD was somewhat different from that of $PM_{2.5}$ concentration. During the

631   study period, the regional mean AOD in the BTH region was 0.78 (Table 4), about twice the

632   long-term observed value of about 0.4 in February and March in the same region (Song et al.,

633   2018).

634   The simulated SSAs were above 0.88 in the BTH region (Figure 6g), with relatively

635   lower values (0.88 - 0.9) in the areas of high $PM_{2.5}$ concentration and higher ones (0.92 - 0.98)

636   in the relatively clean areas. On average, the simulated SSA in the BTH was 0.91 (Table 4),

637   within the range of 0.87 to 0.95 measured in the same region in January 2013 (Che et al.,

638   2014) but slightly lower than the model simulated annual mean of 0.95 over eastern China

639   (Zhuang et al., 2013).

640   All-sky aerosol radiative effects at the surface (ARE_{surf}), at the top of atmosphere

641   (ARE_{TOA}) and in the atmosphere (ARE_{atm}) under all-sky condition are presented in Figures 6h

642   to 6j. During the study period, aerosols induced a negative ARE both at the surface and TOA

643   and a positive ARE in the atmosphere over the BTH. The distribution of ARE resembles that

644   of AOD, generally showing stronger effects over southwestern Hebei, Shanxi and northern

645   Henan provinces where high AOD occurred. Moderate AREs appeared over Beijing, Tianjin

646   and central Hebei, while relatively weak AREs appeared over the northern domain. The

647   domain average AREs in the BTH region during the period were estimated to be -37 W m^{-2},

648   19 W m^{-2} and -18 W m^{-2} at the surface, in the atmosphere and at the TOA, respectively (Table

649   4). The indirect radiative effect was also estimated to be about -2 W m^{2} at the surface and the

650   TOA on average, much smaller than the direct radiative effect; therefore, the total radiative

651   feedback is predominated by direct radiative effect during the study period.

652   The domain average all-sky AREs during the first haze episode (20-26 February) were

653   -57 W m^{-2}, 25 W m^{-2} and -32 W m^{-2} at the surface, in the atmosphere and at the TOA,

654   respectively, and the values were further enhanced to -123 W m^{-2}, 53 W m^{-2} and -70 W m^{-2} in

655   terms of daytime mean. The maximum AREs at the surface and at TOA reached -384 W m^{-2}

656   and -231 W m^{-2}, respectively, at 13:00 LST on 23 February in the vicinity of Shijiazhuang.

657   In Beijing, the estimated mean AREs were -70 W m^{-2}, 32 W m^{-2} and -38 W m^{-2} at the

658   surface, in the atmosphere and at the TOA, respectively, during the first haze episode,

659   whereas the maximum ARE at the surface reached -304 W m^{-2} at 13:00 LST on 22 February,

660   which was associated with the high PM$_{2.5}$ concentration (453 μg m^{-3}) at that time.

661   Based on in-situ surface measurements, Che et al. (2014) estimated that during haze

662   periods in January 2013, the mean daytime AREs at Nanjiao and Xianghe were

663   approximately -42 W m^{-2} and -50 W m^{-2} at TOA, and -120 W m^{-2} at the surface at both sites.

664   In this study, the daytime AREs averaged over the severe haze period (20–26 February) at

665   TOA were estimated to be -77 W m^{-2} and -74 W m^{-2} at Nanjiao and Xianghe, while the

666   corresponding AREs at the surface were -146 W m^{-2} and -140 W m^{-2}, respectively. Che et al.

667   (2014) also reported the maximum daily mean surface ARE of -220 W m^{-2} at Nanjiao during

668   a severe haze episode in January 2013, in this study, the corresponding ARE was estimated to

669   be approximately -200 W m^{-2} at the same site during the severe haze episode in February

670   2014. Therefore, the magnitudes of AREs during haze episodes simulated from this study

671   agreed favorably with the above observational based estimations around Beijing, despite the

672   different time period.

673

674   4.3 Impacts of aerosol radiative feedback on meteorological variables and aerosols

675   Figure 7a–7e shows the mean differences in T2, RH2, wind speed, PBL height and near

676   surface PM$_{2.5}$ concentration induced by the radiative feedback due to all aerosols (FULL

677   minus NoAer) in the domain during the study period.

678   The aerosol radiative effects led to a reduction in surface shortwave radiation and thus

679   surface air temperature in the entire domain. The magnitude of T2 variation decreased from

680   south to north of the BTH, with -1.6 °C to -2 °C in southern Hebei and -1.2 °C to -1.8 °C in

681   southern Beijing, respectively. Correspondingly, RH2 increased by 10%-16% in the above

682   regions. The changes in wind speed showed a patchy pattern, with decreases by ~0.1 m s^{-1} in

683   southern Hebei, increases by ~0.2 m s^{-1} in central Hebei, and decreases in most parts of

684   Beijing. Wind vector shows an anomalous northerly wind of ~0.5 m s^{-1} in the BTH region.

685   Due to the reduction in surface shortwave radiation, PBL height decreased over the entire

686   region, with the maximums up to 240 m in southern Hebei and northern Tianjin. The changes

687   in PBL height varied from -210 m in southern Beijing to -90m in northern Beijing. PM$_{2.5}$

688   concentrations were consistently enhanced over the entire region, with the maximum increase

689   up to 33 μg m^{-3} in southern Hebei and portions of Beijing and Tianjin. In most of the BTH

690   region, the percentage increase of PM$_{2.5}$ exceeded 25%, with the maximum increase

691   exceeding 33% in the vicinity of Shijiazhuang. It is of interest that the regions with the

692   maximum increase of PM$_{2.5}$ generally corresponded to those with the maximum decrease in

693   PBL height. The presence of aerosols reduced solar radiation reaching the ground surface,

694   resulting in decreases in surface air temperature and PBL height and an increase in relative

695   humidity, all of which favored accumulation and formation of aerosols due to weakened

696   vertical mixing and enhanced secondary aerosol formation.

697   The aerosol feedback during the first haze episode was further explored due to the much

698   higher PM$_{2.5}$ level than the period average. Figure 7f–7j show the mean changes in

699   meteorological variables and PM$_{2.5}$ concentrations during the first haze episode (20-26

700   February). In general, the changes induced by aerosol feedback were larger during the severe

701   haze episode than those over the entire study period. T2 decreased by 1.8 °C to 2.7 °C along

702   with an increase up to 20% in RH in southern Hebei and southern parts of Beijing and Tianjin.

703   Different from the entire period average, wind speed decreased consistently in the BTH, with

704   a maximum decrease of 1 m s^{-1}. PBL height decreased by ~300 m in southern Hebei,

705   corresponding to the areas with large air temperature decrease. This resulted in a consistent

706   increase in PM$_{2.5}$ concentrations in the study domain, with the maximum increases exceeding

707   50% around Shijiazhuang and approximately 40% in Beijing and Tianjin, apparently higher

708   than the entire period averages. If for daytime mean, the percentage changes of PM$_{2.5}$ in the

709   above areas increased to 70% and 60%, respectively (figure not shown). It is striking that the

710   simulated maximum increase in hourly PM$_{2.5}$ concentration can be up to 372 μg/m^3 (186%)

711   in the vicinity of Shijiazhuang at about 10:00 LST on 24 February during the first haze

712   episode, which demonstrates the substantial impact of the radiative feedback on $PM_{2.5}$

713   concentration and haze formation.

714   It is worthwhile to further explore the effect of aerosol feedback during haze evolution.

715   We divided haze episode into three stages, the growth stage is defined as the time period of

716     $PM_{2.5}$ increase from clean condition to heavy pollution level, the persistence stage means the

717   duration period of haze and the dissipation stage means the period with a sharp decrease in

718     $PM_{2.5}$ concentration usually along with a cold front passage. During the first heavy haze

719   episode (20–26 February) in Beijing, aerosol radiative feedback caused the increases in $PM_{2.5}$

720   concentration of 55 μg m^{-3}, 84 μg m^{-3} and 40 μg m^{-3}, with the fractional changes of 31%, 41%

721   and 67%, respectively, during the growth, persistence and dissipation stages. The larger

722   fractional change of $PM_{2.5}$ in the dissipation stage is due to the relatively large

723   feedback-induced increase and the lowest $PM_{2.5}$ concentration in the NoAer case in this stage.

724   During the second haze episode (1–4 March), the increases in $PM_{2.5}$ concentration due to

725   aerosol feedback were 25 μg m^{-3}, 45 μg m^{-3} and 24 μg m^{-3}, with the fractional changes of

726   21%, 35% and 34%, respectively, which are lower than the feedback effect during the first

727   haze episode. So, in terms of magnitude, the largest feedback effect on $PM_{2.5}$ occurred in the

728   persistence stage, followed by that in the growth stage, although the fractional change of

729     $PM_{2.5}$ was larger in the dissipation stage.

730   Table 5 summarized the average feedback-induced changes in meteorological variables

731   and $PM_{2.5}$ concentrations over the BTH region during the entire and the first haze periods.

732   During the study period, due to the radiative feedback by all aerosols (FULL minus NoAer),

733   surface air temperature and wind speed decreased by 1.4 °C and 0.04 m s^{-1}, respectively, with

734   RH increased by 8.7% in the BTH. PBL height was reduced by 160 m (or a percentage

735   change of -18.6%) on average, along with a reduction of 3.3 m^2 s^{-1} (-27.0%) in vertical

736   diffusivity coefficient (K_z), resulting in an increase of $PM_{2.5}$ level by 20.0 μg m^{-3} (28.6%). It

737   is noticed that the above changes were strengthened during the severe haze episode on 20–26

738   February, with the 7-day average decreases in T2, WS10, PBL height and K_z being up to -1.8

739   °C, -0.5 m s^{-1}, -183.6 m (-31.0%) and 3.9 m^2 s^{-1} (-48.8%), respectively, and the $PM_{2.5}$

740   concentration increased by 45.1 μg m^{-3} with a percentage increase of 38.7%. Because

741   aerosols affect solar radiation in daytime, in term of daytime mean, the 7-day mean changes

in T2, WS10 and PBL height were estimated to be -2.5 °C, -0.6 m s^{-1} and -307.3 m (-37.6%), respectively, leading to an increase of 49.3 μg m^{-3} (48.5%) in PM$_{2.5}$ concentration.

The impact of aerosol radiative feedback in Beijing (Table 6) was stronger than the regional mean. During the first haze episode, the 7-day average changes in T2, WS10, RH2, PBL and PM$_{2.5}$ were estimated to be -2.1 °C, -0.6 m s^{-1}, 17.0%, -195.6 m (-35.9%) and 68.0 μg m^{-3} (39.1%), respectively, and the daytime mean change in PM$_{2.5}$ concentration increased to 83.2 μg m^{-3} (60%), respectively.

Table 7 presents the average changes in major aerosol components (BC, sulfate and nitrate) in PM$_{2.5}$ induced by the feedback effect. Over the BTH region, the feedback caused the average increases in sulfate and nitrate by 5.0 μg m^{-3} (46.4%) and 6.8 μg m^{-3} (37.3%), respectively, for the entire period, and by up to 12.6 μg m^{-3} (66.9%) and 14.6 μg m^{-3} (40.9%), for the first haze episode. The feedback-induced increases in BC was 0.9 μg m^{-3} (25.1%) and 1.9 μg m^{-3} (32.9%), respectively, for the entire period and the first haze episode. It was noticed that the feedback-induced changes in sulfate and nitrate concentrations were larger than that in BC concentration. This was because that the concentrations of secondary aerosols were increased not only by weakened vertical diffusivity but also by enhanced chemical reactions due to the radiative feedback, which will be discussed in detail in section 5.2.

The above analysis demonstrates a significant impact of aerosol feedback on PM$_{2.5}$ concentration during winter haze episodes in the BTH region. Previous modeling studies reported different degrees of aerosol radiative feedback in east China. Gao et al. (2015) simulated an increase of near surface PM$_{2.5}$ concentrations to be 10-50 μg m^{-3} or 5-25% in the BTH during a severe haze episode on 10-15 January 2013 by using WRF-Chem. For the similar time period and region, Wang et al. (2014a) reported an increase in PM$_{2.5}$ concentrations by 15-50 μg m^{-3} or 10-30% by using a regional coupled model NAQPMS. Wu et al. (2019) used WRF-Chem to investigate a haze episode from 5 December 2015 to 4 January 2016 in the North China Plain and found that the aerosol radiative effects can enhance near-surface PM$_{2.5}$ concentration by 10.2 μg m^{-3} (7.8%) on average.

The results from this study demonstrate a stronger aerosol-radiation feedback than previous modeling studies, with an average increase in PM$_{2.5}$ concentration by up to 45.1 μg m^{-3} (38.7%) during a severe haze episode and further to 49.3 μg m^{-3} (48.5%) for daytime

772 mean over the BTH region. This study also highlights that the aerosol feedback effect can

773 result in an increase of hourly $PM_{2.5}$ concentrations by up to 372 μg m^{-3} (186%) in the

774 vicinity of Shijiazhuang during the severe haze episode. The stronger feedback effect in this

775 study than previous model simulations is mainly due the predicted higher concentration of

776 aerosol components (especially inorganic aerosols) and aerosol optical properties, which are

777 also in a better agreement with observations. It is noticed that a recent study (Zhong et al.,

778 2018a) reported that the aerosol feedback effect contributed over 70% to $PM_{2.5}$ increase

779 during the cumulative explosive stage of haze event in winter Beijing based on integrated

780 analysis of observations from 2013 to 2016, which suggested a dominant role of the feedback

781 effect in haze formation.

782

783 ## 5 Process analysis of haze evolution and aerosol radiative feedback

784   The process analysis (PA) method calculates the Integrated Process Rates (IPRs) and is

785 applied to quantify the individual contributions of different physical and chemical processes

786 to variations of $PM_{2.5}$ and its chemical components. These processes include emission,

787 horizontal and vertical advections (HADV and VADV), horizontal and vertical diffusions

788 (HDIF and VDIF), dry deposition (DDEP), cloud (CLD, including aqueous chemistry and

789 wet scavenging), gas chemistry (GAS), thermodynamic chemistry (Thermo) and

790 heterogeneous chemistry (HET). The focus of this study is Beijing, so the model grid cell

791 near the surface having Beijing is selected for analysis.

792

793 5.1 The mechanism of haze evolution related to various processes

794 5.1.1 Haze evolution during 20–26 February

795   There was a severe haze event lasting for about 7 days, with the maximum hourly $PM_{2.5}$

796 up to 482 μg m^{-3} on 26 February. This haze was initially formed on 20 February, with the

797 observed surface $PM_{2.5}$ concentration less than 50 μg m^{-3} on 19 February, rapidly increased to

798 343 μg m^{-3} on 20 February, and reached 482 μg m^{-3}, followed by rapid haze dissipation on 26

799 February due to the arrival of a cold front.

800   PA was used to provide insights into the evolution mechanism of the haze episode, which

801 was divided into the clean, growth, persistence and dissipation stages in this study. Figure 8

802 shows the average process budgets for changes in $PM_{2.5}$ (which is the sum of sulfate, nitrate,

803 ammonium, BC, OC, SOC and primary $PM_{2.5}$) and its major components in Beijing during

804 the four stages of the first haze period (Figure 8) from the FULL simulation. Figure 8a shows

805 the hourly IPRs of $PM_{2.5}$ by physical and chemical processes. The emission of primary

806 aerosols was the largest contributor to the $PM_{2.5}$ mass with a constant IPR of 29.8 $\mu g\ m^{-3}\ h^{-1}$

807 (not shown in Figure 8a for clarity) due to the use of a monthly based emission inventory.

808 Chemical processes (GAS, Thermo and HET) also contributed largely to $PM_{2.5}$, with

809 generally larger contributions in the growth and persistence stages. Thermodynamic

810 equilibrium processes and gas chemistry accounted for over 2/3 of the chemical contributions,

811 with the former process mainly accounting for the formation of nitrate and ammonium and

812 the latter one for sulfate formation. The contribution from heterogeneous reactions was

813 generally small, but when conditions were favorable (such as high RH and high aerosol

814 concentration providing sufficient reaction surfaces), its contribution would also be

815 significant, such as on the morning of 22 February, at nighttime from 23 to 24 February, and

816 on the mornings of 25 and 26 February. Vertical diffusion and dry deposition consistently

817 removed $PM_{2.5}$ from the atmosphere. In general, the larger IPRs from both VDIF and DDEP

818 during the clean and dissipation stages resulted in lower $PM_{2.5}$ concentrations, whereas the

819 lower IPRs from VDIF and DDEP in the growth stage favored aerosol accumulation. In the

820 persistence stage, the IPRs of VDIF and DDEP were generally small. It should be noted that

821 on every midday, when PBL was fully developed, the vertical diffusion reached the daily

822 maximum, producing distinctly large negative IPRs of VDIF. Advections (HADV and VADV)

823 and horizontal diffusion either contributed to the accumulation or loss of $PM_{2.5}$. During this

824 severe haze episode, horizontal diffusion served as a sink of $PM_{2.5}$, producing a negative IPR

825 of HDIF through the event. Horizontal advection served as a sink of $PM_{2.5}$ in most of the time,

826 leading to a negative IPR of HADV, however, when the removal of $PM_{2.5}$ by vertical

827 diffusion was strong at the midday, aerosols were advected to Beijing from surrounding areas

828 due to mass balance, resulting in a positive IPR of HADV. The positive IPR of VADV during

829 the growth and persistence stages of this event indicated that the downward transport of

830 aerosols from upper levels also contributed to the $PM_{2.5}$ increase, such as on the mornings of

831 22 and 25 February. In general, the IPRs (represented the net effect of all processes, denoted

832 by the red line in Figure 8a) exhibited small positive values from evening to next morning on

833 every day, indicating a gradually increasing $PM_{2.5}$ concentration, whereas on every midday,

834 relatively large negative IPRs occurred, indicating an apparent decrease in $PM_{2.5}$

835 concentration at that time. It should be mentioned that even in the persistence stage, the

836 diurnal variation of $PM_{2.5}$ occurred although the change rates were generally weaker than

837 those in the growth and dissipation stages.

838 Figure 8b to 8f show the mean IPRs for $PM_{2.5}$ and its major chemical components as well

839 as the key meteorological variables averaged over each stage to help interpret the formation

840 and evolution mechanism of this severe haze episode.

841 In the clean stage, emission and chemistry were the two major processes for $PM_{2.5}$

842 production (Figure 8b). Emission contributed predominately to $PM_{2.5}$ production (IPRs of

843 29.8 $\mu g \ m^{-3} \ h^{-1}$), whereas the contributions of gas (9.2 $\mu g \ m^{-3} \ h^{-1}$) and thermodynamic

844 chemistry (7.3 $\mu g \ m^{-3} \ h^{-1}$) were comparable. The most influential process for $PM_{2.5}$ removal

845 was vertical diffusion, with the IPRs of -30.3 $\mu g \ m^{-3} h^{-1}$, comparable to that of emission. Dry

846 deposition was the second most important process for $PM_{2.5}$ loss (-12.2 $\mu g \ m^{-3} \ h^{-1}$), followed

847 by horizontal diffusion. Advection had a negligible effect on $PM_{2.5}$ in this stage. In the growth

848 stage, it is noteworthy that the contributions from vertical diffusion (VDIF) and dry

849 deposition (DDEP) to $PM_{2.5}$ removal decreased markedly from -30.3 $\mu g \ m^{-3} \ h^{-1}$ and -12.2 μg

850 $m^{-3} \ h^{-1}$ in the clean stage to -21.6 $\mu g \ m^{-3} \ h^{-1}$ and -9.2 $\mu g \ m^{-3} \ h^{-1}$, respectively (Figure 8b),

851 mainly due to the decrease in wind speed and the increase in stability indicated by the

852 reduced vertical diffusivity coefficient K_z (Figure 8f), leading to increases in concentrations

853 of all species. It is impressive that the contributions from chemical processes

854 (GAS+Thermo+HET) increased apparently compared with those in the clean stage, with the

855 IPRs from gas, thermodynamic and heterogeneous chemistry increase to 12.1 $\mu g \ m^{-3} \ h^{-1}$, 16.0

856 $\mu g \ m^{-3} \ h^{-1}$ and 5.4 $\mu g \ m^{-3} \ h^{-1}$, respectively. The increase in the contribution from

857 heterogeneous chemistry was mainly attributed to the increase in relative humidity and

858 aerosol surfaces, upon which heterogeneous reactions took place. It is noticed that the

859 contribution of thermodynamic chemistry increased with increasing relative humidity as well

860 along with haze formation (Figure 8f). The increase in the contribution of thermodynamic

861   chemistry was remarkable (with IPR from 7.3 to 16 µg m^{-3} h^{-1}), because gas precursors of

862   aerosols increased due to weakened vertical diffusivity and higher relative humidity during

863   haze period favored condensation from gas to aerosol phase. It is of interest that vertical

864   advection also contributed to PM$_{2.5}$ production (IPR of 5.4 µg m^{-3} h^{-1}) in this stage, which

865   indicated a potential downward import of PM$_{2.5}$ from upper layer. It is also noticed that

866   horizontal advection contributed to PM$_{2.5}$ loss (-12.8 µg m^{-3} h^{-1}). This is because the strong

867   gradient between the increased PM$_{2.5}$ level in Beijing caused by weakened vertical diffusivity

868   and the relatively lower PM$_{2.5}$ level in the surrounding areas, which led to an outflow of

869   PM$_{2.5}$. In the growth stage, the net variation rate (IPR) of PM$_{2.5}$ concentration was 14.1 µg

870   m^{-3} h^{-1}, in which emissions, chemical processes (GAS+Therm+HET) and physical processes

871   (HADV+VADV+HDIF+VDIF+DDEP) contributed 29.8 µg m^{-3} h^{-1}, 33.5 µg m^{-3} h^{-1} and -49.2

872   µg m^{-3} h^{-1}, respectively. In the persistence stage, chemical production rate of PM$_{2.5}$ changed

873   slightly, and the production and loss rates of PM$_{2.5}$ were similar, leading to an approximately

874   zero IPR in this stage (Figure 8b). In the dissipation stage, the contribution of vertical

875   diffusion and dry deposition to PM$_{2.5}$ loss increased largely, while the total chemical

876   production rate decreased, which resulted in a net IPR of -34.8 µg m^{-3} h^{-1}, indicating a

877   substantial decrease in PM$_{2.5}$ concentration (Figure 8b). It was also noticed that HADV

878   contributed to PM$_{2.5}$ production in this stage, which was due to mass import to Beijing from

879   upwind areas by northwesterlies.

880   It should be mentioned that the contribution of emission was unchanged because the

881   monthly based emission inventory from MEIC was used, and the contribution of cloud

882   process was generally negligible throughout the period because there was little cloud and

883   precipitation during the study period.

884   We further use PA to interpret evolution processes of primary (BC) and secondary

885   (sulfate and nitrate) aerosols.

886   Black carbon is considered to be inert and chemical inactive, so it is governed solely by

887   physical processes. In the clean stage, BC production was contributed solely by emission (5.7

888   µg m^{-3} h^{-1}), whereas vertical diffusion and dry deposition contributed equally to BC loss (-2.7

889   µg m^{-3} h^{-1}), and other processes were negligible (Figure 8c). In the growth stage, the

890   contribution of vertical diffusion and dry deposition to BC loss decreased to -2.0 µg m^{-3} h^{-1}

and -1.7 μg m^{-3} h^{-1}, respectively, and the net rate of change was 0.7 μg m^{-3} h^{-1}, indicating a rapid increase of BC concentration in this stage (Figure 8c). In the persistence stage, the loss rate by vertical diffusivity and dry deposition further increased mainly due to the increased BC concentration (Figure 8c). It is noticed that horizontal advection somewhat contributed to the loss of BC (-0.7 μg m^{-3} h^{-1}), which indicated an increasing outflow of BC to surrounding areas. The IPR was near zero, indicating a balance of production and loss rate in this stage. In the dissipation stage, BC loss via vertical diffusion and dry deposition processes increased largely, mainly due to increasing wind speed and vertical diffusivity, and the net IPR became -1.6 μg m^{-3} h^{-1}. This absolute value was larger than that in the growth stage (0.7 μg m^{-3} h^{-1}), which indicated a faster decrease in BC concentration than the BC increase in the growth stage (Figure 8c).

As for secondary aerosols, like sulfate, contribution from direct emission was near zero. In the clean stage, gas chemistry (5.9 μg m^{-3} h^{-1}) was the predominant process for sulfate production, and vertical diffusion contributed most to the loss (-5.2 μg m^{-3} h^{-1}) (Figure 8d). In the growth stage, contribution from vertical diffusion was reduced to -3.9 μg m^{-3} h^{-1} mainly due to the decreased vertical diffusivity (Figure 8f), whereas positive contribution from gas chemistry increased to 6.6 μg m^{-3} h^{-1}, which was resulted from competitive processes. For sulfate formation from gas chemistry ($SO_2+OH\rightarrow H_2SO_4$), the oxidation of SO_2 to sulfate was weakened because of decreasing OH radical due to increasing aerosol attenuation of solar radiation, however, SO_2 increased due to weakened vertical diffusivity, leading to a slight net increase of sulfate concentration compared with the clean stage. It is noteworthy that the sulfate production rate from heterogeneous reactions increased to 2.7 μg m^{-3} h^{-1}, mainly due to the increases in SO_2, aerosol surfaces and RH (as well as aerosol water content). All the processes led to a net sulfate production rate of 2.7 μg m^{-3} h^{-1}, in which chemistry played a predominant role (IPR of 9.3 μg m^{-3} h^{-1}). In the persistence stage, the contribution of gas and heterogeneous processes further increased to 7.4 μg m^{-3} h^{-1} and 4.3 μg m^{-3} h^{-1}, indicating an increasing sulfate production through chemical processes (Figure 8d). It is interesting to note that vertical diffusion contributed more to sulfate loss than in the growth stage, which was mainly due to the higher sulfate level than in the growth stage while vertical diffusivity coefficients were almost the same. The net IPR in this stage was just 0.2 μg m^{-3} h^{-1}, which

921 indicated an approximate balance of production and loss. In the dissipation stage, increasing

922 vertical diffusivity was the dominant process for sulfate loss, and chemical contribution

923 decreased. It is noticed a positive contribution to sulfate from horizontal advection (IPR of

924 4.3 μg m^{-3} h^{-1}), which was due to an import of sulfate from upwind areas of Beijing by

925 northwesterly winds, like those for PM$_{2.5}$ and BC.

926 For nitrate, in the clean stage, thermodynamic process (4.5 μg m^{-3} h^{-1}) was the largest

927 contributor to nitrate production (Figure 8e). During the growth stage, the contribution of

928 thermodynamic processes (10.2 μg m^{-3} h^{-1}) increased by over a factor of two and was larger

929 than the contribution from heterogeneous process (Figure 8e). The substantial increase in the

930 contribution of thermodynamic processes to nitrate production was due to the combined

931 effects of the increased level of nitrate precursors (HNO$_3$ and NH$_3$) resulting from weakened

932 diffusivity and the increased RH along with the decreased air temperature, which were

933 favorable for gas to aerosol conversion. The contribution of heterogeneous reactions

934 increased as well due to the increased aerosol surface and relative humidity. The net rate of

935 nitrate change in this stage was 5.3 μg m^{-3} h^{-1}. In the persistence stage, the contribution from

936 heterogeneous reactions changed slightly while the contribution from thermodynamic process

937 somewhat reduced (Figure 8e). This is because more NH$_3$ was consumed to neutralize the

938 increased sulfate, leaving less NH$_3$ to react with HNO$_3$, and thus producing fewer nitrate. The

939 near zero net IPR of nitrate in this stage also indicated a balance of production and loss. In

940 the dissipating stage, the contribution of chemical processes was almost the same as that in

941 the clean stage, while physical processes dominated the loss and the net IPR of nitrate (Figure

942 8e).

943

944 5.1.2 Haze evolution during 1–4 March

945 We also investigate another haze period of 1–4 March using PA (Figure 9). The hourly

946 IPRs by different processes are shown in Figure 9a. An apparent difference between this

947 episode and the first one was the positive IPRs of HADV during this episode, especially in

948 the growth stage from 21:00 (LST) on 1 March to 9:00 (LST) on 2 March, which indicated

949 that horizontal transport contributed to the haze formation. Another difference is that the

950 chemical processes, especially heterogeneous reactions contributed less to the PM$_{2.5}$ mass

951 during the persistence stage, such as from 10:00 (LST) on 2 March to 3:00 (LST) on 4 March,

952 which will be discussed below.

953   The IPRs for PM$_{2.5}$ and its components and meteorological variables averaged over each

954 stage during this episode are calculated and presented in Figure 9b to 9f. For BC (Figure 9c),

955 the most evident difference from the first haze episode occurred in the growth stage, in which

956 horizontal advection contributed 1.5 μg m^{-3} h^{-1} to BC production, which was comparable in

957 magnitude to the negative contributions from vertical diffusion and dry deposition (-1.3 μg

958 m^{-3} h^{-1}), suggesting the import of BC into Beijing from surrounding areas. The wind direction

959 in the south of Beijing at this stage was southerly and wind speed was about 2-3 m s^{-1}, so the

960 transport of pollutants from southern Hebei apparently contributed to the increase of BC level

961 in Beijing. Differently, during the first haze event on 20–26 February, wind direction was

962 easterly, bringing less polluted air mass from the Bohai Sea and northern Tianjin, so

963 horizontal advection contributed less to BC in Beijing. This transport feature was also

964 reflected in the change rates of sulfate (Figure 9d), nitrate (Figure 9e) and PM$_{2.5}$ (Figure 9b)

965 concentrations. An observational study for the same haze period in Beijing (Ma et al., 2017)

966 also suggested the important role of regional transport from the south of Beijing in haze

967 formation.

968   For sulfate (Figure 9d), although chemical processes still contributed most to sulfate

969 production in the growth stage (6.0 μg m^{-3} h^{-1}), it is noticed that gas chemistry (5.9 μg m^{-3} h^{-1})

970 accounted for most of the sulfate production, whereas contribution from heterogeneous

971 reactions was smaller than that in the first haze episode mainly due to lower relative humidity.

972 In the growth stage, the net IPR was 1.9 μg m^{-3} h^{-1}, 30% smaller than that for the first haze,

973 indicating a weaker secondary aerosol formation during this haze episode. In the persistence

974 stage, sulfate production from gas phase oxidation was almost balanced by the loss from dry

975 deposition and vertical diffusion, resulting in a net IRP of -0.1 μg m^{-3} h^{-1}, indicating a small

976 variation of sulfate concentration during this stage on average.

977   For nitrate, in the growth stage, it is of interest to note that heterogeneous reactions (5.5

978 μg m^{-3} h^{-1}) dominated over thermodynamic processes (2.7 μg m^{-3} h^{-1}) in nitrate formation,

979 which could be due to the low RH in this stage. Fountoukis and Nenes (2007) indicated that

980 nitrate aerosol is hardly formed in the ISORROPIA II model when RH is below 40%. The

average RH is about 37% during this haze episode, resulting in more nitrate formed by heterogeneous reactions. The net IPR in the growth stage was 3.7 μg m^{-3} h^{-1}, approximately 30% smaller than that in the first haze episode. In the persistence stage when relative humidity increased to 51%, nitrate formation via thermodynamic processes became important, and due to competition, nitrate formation from heterogeneous reactions was reduced.

For PM$_{2.5}$ (Figure 9b), in the growth stage, the IPR of PM$_{2.5}$ concentration was 13.0 μg m^{-3} h^{-1}, in which emission, chemical processes (GAS+Therm+HET) and physical processes (HADV+VADV+HDIF+VDIF+DDEP) contributed 29.8 μg m^{-3} h^{-1}, 23.9 μg m^{-3} h^{-1} and -40.7 μg m^{-3} h^{-1}, respectively. It is noteworthy that horizontal advection process (HADV) contributed 22.4 μg m^{-3} h^{-1} to PM$_{2.5}$ production in this episode, which was comparable to the total chemical production of 23.9 μg m^{-3} h^{-1}. This reveals the comparable contributions to PM$_{2.5}$ in Beijing from local sources and regional transport during this haze episode. In the persistence stage, because of the change in wind direction and lower wind speed, the regional transport of PM$_{2.5}$ became weak. The IPRs were -4.0 μg m^{-3} h^{-1} for HADV and 1.2 μg m^{-3} h^{-1} for VADV, respectively, which were obviously smaller than those in the first haze episode. In the dissipation stage, physical processes except HADV all contributed to the loss of PM$_{2.5}$. Compared with the first haze episode, the negative IPR of VADV decreased mainly due to the larger wind speeds in this episode, as more PM$_{2.5}$ was removed by VADV, the remaining PM$_{2.5}$ loss by vertical diffusion decreased, consequently a weakened VDIF. The positive IPR of HADV increased as well due to larger wind speed than that in the first episode in this stage.

The above process analyses reveal that for the first haze episode (20–26 February) in Beijing, local emissions and chemical processes were the main contributors to the formation and persistence of the haze event. However, for the second haze (1–4 March), regional transport or horizontal advection played a more important role in haze formation, with a similar magnitude to local emissions and chemical productions in the growth stage. In all, for both episodes, local emission, chemical reaction and horizontal advection were major processes contributing to PM$_{2.5}$ increase, whereas vertical processes (diffusion, dry deposition and advection) were major processes for PM$_{2.5}$ removal. As the pollution level increased, the contribution of secondary aerosols through chemical formation to PM$_{2.5}$ increased apparently

1011 in Beijing.

1012

1013 5.2 Contributions of physical and chemical processes to the aerosol feedback

1014 5.2.1 The first haze episode (20–26 February)

1015   Figure 10 shows the contributions of each process to the feedback-induced difference in

1016 the change rates of $PM_{2.5}$ and its major components (ΔIPR) during the first haze episode (20–

1017 26 February), which were derived from the difference between cases with and without

1018 aerosol radiative effects (FULL minus NoAer).

1019   The definition of the four stages during haze evolution is the same as that in section 5.1.1.

1020 For BC (Figure 10b) in the clean stage, the aerosol feedback caused a decrease in vertical

1021 diffusion and advection (Figure 10e), leading to an increase in BC concentration with the

1022 ΔIPR of 0.40 $\mu g \ m^{-3} \ h^{-1}$ from VDIF+VADV, concurrently, the feedback caused an increased

1023 loss of BC through horizontal diffusion (HDIF) and advection (HADV) and dry deposition

1024 (DDEP) due to the increased BC concentration, with the ΔIPR of -0.39 $\mu g \ m^{-3} \ h^{-1}$ from

1025 HADV+HDIF+DDEP (Figure 10b). The net ΔIPR was near zero, which indicated a

1026 negligible feedback effect during the clean stage. In the growth stage, the feedback caused a

1027 pronounced decrease in vertical diffusivity, advection, as well as dry deposition velocity,

1028 leading to apparent increases in BC level, with the contributions to ΔIPRs from VDIF, VADV,

1029 and DDEP being 0.50 $\mu g \ m^{-3} \ h^{-1}$, 0.50 $\mu g \ m^{-3} \ h^{-1}$ and 0.20 $\mu g \ m^{-3} \ h^{-1}$, respectively (Figure

1030 10b). The increase in BC concentration consequently led to an increase in outflow via HADV

1031 and HDIF, with the ΔIPRs of -0.63 $\mu g \ m^{-3} \ h^{-1}$ and -0.12 $\mu g \ m^{-3} \ h^{-1}$, respectively, which tended

1032 to reduce BC concentration. The total effect by summing the processes exhibited a net

1033 positive ΔIPR of 0.44 $\mu g \ m^{-3} \ h^{-1}$, which indicated an apparent increase in BC concentration

1034 due to the feedback. In the persistence stage, the sign of ΔIPR for each process was the same

1035 as that in the growth stage, and the ΔIPR by vertical processes (0.84 $\mu g \ m^{-3} \ h^{-1}$ from

1036 VADV+VDIF+DDEP) was generally balanced by that of horizontal processes (-0.80 $\mu g \ m^{-3}$

1037 h^{-1} from HADV+HDIF) and led to a net ΔIPR of 0.04 $\mu g \ m^{-3} \ h^{-1}$ (Figure 10b), which

1038 indicated the difference in the BC change rate between the FULL and NoAer cases was small

1039 in this stage. In the dissipating stage, the ΔIPRs were negative for all the processes except for

1040 HADV. This was because of the higher BC levels due to the feedback, which caused more

1041 BC to be removed than without feedback, although the vertical diffusion coefficient was

1042 smaller due to the feedback. The positive ΔIPR from HADV suggested the enhanced BC

1043 import into Beijing from upwind regions due to the feedback. The sum of these processes

1044 produced a net ΔIPR of -1.20 μg m^{-3} h^{-1}, which indicated a larger decreasing rate of BC

1045 concentration (from haze to clean level) due to aerosol feedback in this stage.

1046   For sulfate (Figure 10c), in the clean stage, the feedback-induced changes were as small

1047 as those for BC. In the growth stage, besides the positive ΔIPRs by VDIF, VADV and DDEP

1048 as those for BC, the most impressive feature was the larger contributions from GAS and HET,

1049 with the ΔIPRs being 0.29 μg m^{-3} h^{-1} and 1.73 μg m^{-3} h^{-1}, respectively, much larger than those

1050 (0.11 μg m^{-3} h^{-1} and 0.23 μg m^{-3} h^{-1}) in the clean stage because of the increased gas

1051 precursors, aerosol surfaces and RH due to the feedback effect, which enhanced chemical

1052 formation (Figure 10c, 10e). The sum of the ΔIPRs by all the processes was 1.92 μg m^{-3} h^{-1},

1053 indicating an apparent increase in sulfate concentration due to the feedback effect. In the

1054 persistence stage, the ΔIPRs by GAS and HET increased. However, the ΔIPR of VDIF

1055 became negative, which could be explained by the increased sulfate concentration due to

1056 aerosol feedback caused more sulfate to be removed through vertical diffusion, leading to a

1057 negative ΔIPR of VDIF, although the vertical diffusion coefficient was reduced by the

1058 feedback. In the dissipation stage, the ΔIPR by HET decreased because the feedback-induced

1059 differences in the concentrations of precursors and aerosols became smaller. The large

1060 negative ΔIPR by VDIF indicated a larger decreasing rate in sulfate concentration from the

1061 persistence to clean stages due to the feedback.

1062   For nitrate (Figure 10d), the feedback-induced IPR changes in the clean stage were

1063 similar to those for sulfate. In the growth stage, remarkable increases in nitrate formation

1064 from Thermo and HET processes occurred, with the ΔIPRs of 3.30 μg m^{-3} h^{-1} and 0.50 μg m^{-3}

1065 h^{-1}, respectively (Figure 10d). The increased gas precursors and RH due to the aerosol

1066 feedback reinforced chemical formation processes. In this stage, the overall ΔIPR was 3.90

1067 μg m^{-3} h^{-1}, suggesting a faster increasing rate in nitrate concentration in consideration of

1068 aerosol feedback. In the persistence stage, the ΔIPR by Thermo was smaller than that in the

1069 growth stage (Figure 10d). This could be explained that the apparent increase in sulfate

1070 concentration via HET and GAS due to the feedback (Figure 10c) in this stage consumed

1071   more ammonia, which inhibited the formation of nitrate ammonium via thermodynamic

1072   processes. The net ΔIPR by all the processes in this stage was near zero, which indicated that

1073   the radiative feedback exerted little effect on the change rate of nitrate concentration during

1074   this stage. In the dissipation stage, the attenuation of solar radiation by aerosols was

1075   weakened because of the decrease in aerosol concentration, meanwhile, the concentrations of

1076   gas precursors (NO_x) were elevated due to the feedback, the combined effect resulted in an

1077   increase of photochemical production of HNO_3; in addition, RH was increased due to the

1078   feedback as well, as a result, nitrate formation via thermodynamic process was enhanced,

1079   leading to a positive ΔIPR of 3.73 $\mu g\ m^{-3}\ h^{-1}$ by Thermo in this stage.

1080   For $PM_{2.5}$, the net ΔIPR due to aerosol feedback in the clean stage was 0.30 $\mu g\ m^{-3}\ h^{-1}$, in

1081   which 1.22 $\mu g\ m^{-3}\ h^{-1}$ was from chemical processes (GAS+Thermo+HET) and -0.90 $\mu g\ m^{-3}$

1082 h^{-1} from physical processes (HADV+VADV+HDIF+VDIF+DDEP) (Figure 10a). In the

1083   growth stage, the net ΔIPR was 9.50 $\mu g\ m^{-3}\ h^{-1}$, which meant in every hour, approximate 9.50

1084 $\mu g\ m^{-3}$ of $PM_{2.5}$ mass was elevated in Beijing due to the feedback effect. The above

1085   feedback-induced difference in the change rate of $PM_{2.5}$ (ΔIPR) resulted from a combined

1086   effect from chemical processes (7.27 $\mu g\ m^{-3}\ h^{-1}$) and physical processes (2.23 $\mu g\ m^{-3}\ h^{-1}$),

1087   which suggested that chemical processes contributed more to the $PM_{2.5}$ increase than physical

1088   processes. However, it was noted that the increased contribution from chemical processes

1089   was related to increasing gas precursors, which was partly associated with physical processes.

1090   It was noteworthy that the positive ΔIPRs were contributed by both chemical processes (GAS,

1091   Thermo and HET) and vertical movements (VADV, VDIF and DDEP) (Figure 10a). The sum

1092   of positive ΔIPRs was 22.88 $\mu g\ m^{-3}\ h^{-1}$, in which 7.27 $\mu g\ m^{-3}\ h^{-1}$ was from chemical

1093   processes and 15.61 $\mu g\ m^{-3}\ h^{-1}$ from vertical movements. This suggested a larger

1094   feedback-induced $PM_{2.5}$ increase through vertical movements than via chemical processes.

1095   However, the outflow (HADV+HDIF) of $PM_{2.5}$ was also enhanced due to the increased $PM_{2.5}$

1096   level by aerosol feedback, producing a negative ΔIPR (-13.38 $\mu g\ m^{-3}\ h^{-1}$), and partly

1097   offsetting the positive ΔIPR (15.61 $\mu g\ m^{-3}\ h^{-1}$) by vertical movements, resulting in a net ΔIPR

1098   of 2.23 $\mu g\ m^{-3}\ h^{-1}$ from all the physical processes. In the persistence stage, the sign of ΔIPRs

1099   by different processes generally resembled those in the growth stage except that of VDIF

1100   whose ΔIPR was negative, which indicated more removal though VDIF mainly due to the

increased secondary aerosol concentrations by aerosol feedback. The net ΔIPR by all the processes was 0.40 μg m^{-3} h^{-1} in this stage, indicating a small influence of aerosol feedback on the change rate of PM$_{2.5}$ concentration. In the dissipating stage (Figure 10a), the large negative ΔIPR from VDIF indicated more PM$_{2.5}$ mass was removed via vertical diffusion while considering aerosol feedback, although the feedback induced a smaller vertical diffusivity coefficient. The net ΔIPR of -24.60 μg m^{-3} h^{-1} indicated a larger decreasing rate of PM$_{2.5}$ concentration in the FULL case than in the NoAer case.

5.2.2 The second haze episode (1–4 March)

For BC in the second haze episode (1–4 March), the most obvious difference from the first episode was in the growth stage, in which the ΔIPR by horizontal advection (HADV) was 0.70 μg m^{-3} h^{-1} (Figure 11b). The radiative feedback led to a weakened vertical diffusivity and a decreased PBL height (Figure 11e), which favored the accumulation of BC and caused a positive ΔIPR of 0.40 μg m^{-3} h^{-1} from VDIF. The wind direction in the growth stage was southerlies as discussed above, bringing aerosols from the south to Beijing. The aerosol feedback enhanced BC concentration in source regions through reducing vertical diffusivity, leading to an increased northward flux of BC and a positive ΔIPR from HADV. The higher BC concentration due to the feedback via HADV and VDIF consequently led to an increase in BC outflow out of Beijing via vertical advection (VADV) and horizontal diffusion (HDIF), with the ΔIPRs of -0.60 μg m^{-3} h^{-1} and -0.20 μg m^{-3} h^{-1}, respectively. In this stage, the net ΔIPR of BC was 0.20 μg m^{-3} h^{-1}, in which 0.50 μg m^{-3} h^{-1} was from horizontal movements (HADV+HDIF) and -0.30 μg m^{-3} h^{-1} from vertical movements (VADV+VDIF+DDEP), indicating that the feedback effect strengthened the contribution of horizontal movements to surface BC concentration in Beijing. In the persistence stage (Figure 11b), the net ΔIPR was also near zero (-0.02 μg m^{-3} h^{-1}), indicating that the BC change rate was merely affected by the feedback in this stage. In the dissipation stage (Figure 11b), the ΔIPRs were negative for all the processes except for VDIF. This could be attributed to the higher BC levels due to the feedback, which caused more BC to be removed than without feedback through these processes. The net ΔIPR was -0.17 μg m^{-3} h^{-1}, the same as that in the growth stage, but with opposite sign.

For sulfate (Figure 11c), in the growth stage, different from the relatively large positive ΔIPR by chemical processes in the first haze episode, the feedback caused small IPR changes via chemical production because SO_2 concentration in this episode was lower than that in the first one and sulfate was mainly formed in upwind regions and transported to Beijing. Consequently, relatively large sulfate increases through HADV and VDIF in this episode. In this stage, the feedback caused a slight increase in sulfate concentration by GAS with ΔIPR of 0.17 μg m^{-3} h^{-1} due to slightly elevated precursors, however, because of the low relative humidity (mean RH was 38%) and competitive processes, heterogeneous reactions were depressed. In terms of physical processes, due to the feedback effect, horizontal transport (HADV) was strengthened (ΔIPR of 1.0 μg m^{-3} h^{-1}) due to the increased sulfate concentration to the south of Beijing, meanwhile, the weakened vertical diffusivity caused an increase in sulfate concentration by VDIF and DDEP, with the ΔIPRs of 1.0 μg m^{-3} h^{-1} and 0.57 μg m^{-3} h^{-1}, respectively, consequently, the outflow of sulfate out of Beijing was also increased via vertical advection (VADV) and horizontal diffusion (HDIF). The net ΔIPR in the growth stage was 0.90 μg m^{-3} h^{-1}, indicating an apparent increase in sulfate concentration due to the feedback. In the persistence stage, the ΔIPRs by GAS and HET changed slightly compared with those in the growth stage. The negative ΔIPR by VDIF indicated more loss of sulfate by vertical diffusion while considering aerosol feedback. The net ΔIPR in this stage was 0.02 μg m^{-3} h^{-1}, indicating a negligible feedback effect on sulfate change rate in this stage. In the dissipation stage, the feedback-induced higher sulfate concentration caused more removal of sulfate via physical processes except HADV, resulting in a net ΔIPR of -0.64 μg m^{-3} h^{-1}. The positive ΔIPR from HADV was due to the strengthened import from upwind areas due to the feedback.

For nitrate, in the growth stage, the feedback also induced an increase in nitrate concentration via horizontal advection like sulfate (Figure 11d). The increases in gas precursors and aerosol surfaces due to the feedback enhanced nitrate formation, resulting in nitrate increases via Thermo and HET, with the ΔIPRs of 0.88 μg m^{-3} h^{-1} and 0.46 μg m^{-3} h^{-1}, respectively. To the persistence stage, the chemical production of nitrate increased largely caused by the feedback, with the ΔIPR of Thermo being 4.30 μg m^{-3} h^{-1}. The reason could be the low RH in the growth stage (38% shown in Figure 9f) left most of nitric acid remained in

1161 gas phase together with the increase in RH due to the feedback (13.2% shown in Figure 11e)

1162 drove its conversion from gas to aerosol phase. Due to the enhanced thermodynamics

1163 production, nitrate formation via heterogeneous reactions was depressed in this stage. The

1164 increased nitrate concentration via Thermo led to larger removal via vertical diffusion,

1165 resulting in a negative ΔIPR of -4.80 μg m^{-3} h^{-1} by VDIF, and a net ΔIPR of -0.10 μg m^{-3} h^{-1}.

1166 In the dissipation stage, like that in the first haze episode, the reduced aerosol attenuation of

1167 solar radiation and increased RH induced by aerosol feedback led to an increase in nitrate via

1168 thermodynamic process, with the ΔIPR of 1.80 μg m^{-3} h^{-1} by Thermo. Consequently,

1169 heterogeneous reactions were depressed due to competitive processes (ΔIPR of -0.97 μg m^{-3}

1170 h^{-1} by HET). In this stage, because of the higher nitrate concentration, the feedback led to

1171 larger removal by vertical processes (the ΔIPR of VADV+VDIF+DDEP was -3.23 μg m^{-3} h^{-1}),

1172 with a net ΔIPR of -1.78 μg m^{-3} h^{-1}, similar to the ΔIPR in the growth stage but with opposite

1173 sign.

1174   For PM$_{2.5}$ (Figure 11a), the net ΔIPR due to aerosol feedback in the growth stage was

1175 2.40 μg m^{-3} h^{-1}, with 1.40 μg m^{-3} h^{-1} from physical processes

1176 (HADV+VADV+HDIF+VDIF+DDEP) and 1.0 μg m^{-3} h^{-1} from chemical processes

1177 (GAS+Thermo+HET), which indicated that the feedback-induced increase in PM$_{2.5}$

1178 concentration per hour was produced through larger contributions from physical processes

1179 than chemical processes in this episode. HADV contributed most to the PM$_{2.5}$ increase (with

1180 ΔIPR of 10.20 μg m^{-3} h^{-1}), followed by VDIF (with ΔIPR of 2.90 μg m^{-3} h^{-1}). As mentioned

1181 above, the weakened vertical diffusivity caused by the feedback enhanced aerosol

1182 concentrations in the entire BTH region, meanwhile, the feedback induced a southeast wind

1183 anomaly with a slight change in wind speed in the regions south of Beijing. The combined

1184 effect of the elevated aerosol concentrations and southeast wind anomaly brought more

1185 aerosols to Beijing. In the persistence stage, the feedback increased PM$_{2.5}$ concentration

1186 mainly through chemical processes, with the ΔIPR of 6.05 μg m^{-3} h^{-1}, which was mainly

1187 resulted from the enhanced thermodynamic production of ammonium nitrate, and such

1188 increase in aerosol mass due to feedback led to more aerosols to be diffused than that without

1189 feedback, leading to the ΔIPR of -7.30 μg m^{-3} h^{-1} by VDIF. It is noticed that the signs of the

1190 ΔIPRs by VDIF were opposite between the growth and persistence stages even though the

1191   vertical diffusivities were both decreased. In the growth stage, the $PM_{2.5}$ concentration was

1192   gradually increasing, the effect of the weakened vertical diffusivity was dominated, resulting

1193   in a positive ΔIPR by VDIF which favored further accumulation of aerosols; in the

1194   persistence stage, the aerosol concentration had already been elevated to a high level, the

1195   effect of higher concentration surpassed that of weakened vertical diffusivity due to the

1196   feedback and led to a negative ΔIPR, which meant the feedback caused more loss of $PM_{2.5}$

1197   via VDIF. In the persistence stage, the net ΔIPR was 0.44 μg m^{-3} h^{-1}, in which -5.6 μg m^{-3} h^{-1}

1198   from physical processes and 6.05 μg m^{-3} h^{-1} from chemical processes, which indicated the

1199   feedback-induced overall changes in the change rate of $PM_{2.5}$ concentration in this stage were

1200   relatively small. In the dissipating stage, the removal of $PM_{2.5}$ was enhanced by the feedback

1201   through all the processes except HADV mainly due to the increased $PM_{2.5}$ concentration, the

1202   positive ΔIPR by HADV was caused by the enhanced import from upwind areas due to the

1203   feedback. In this stage, the feedback effect enhanced the removal of $PM_{2.5}$, which was

1204   reflected by the net negative ΔIPR of -4.30 μg m^{-3} h^{-1}.

1205   The above analyses quantify the key processes contributing to the aerosol radiative

1206   feedback in Beijing during the two haze episodes. In the growth stage of the first haze

1207   episode, the feedback-induced $PM_{2.5}$ enhancement was attributed to the positive contributions

1208   from chemical processes and vertical movements, but partly offset by the increased outflow

1209   of $PM_{2.5}$ via horizontal advection, resulting in a larger increase in $PM_{2.5}$ through chemical

1210   processes than that from physical processes. Differently, duirng the second haze episode, the

1211   feedback-induced $PM_{2.5}$ enhancement in the growth stage was larger by physical processes

1212   than that by chemical processes, and horizontal advection contributed most to the $PM_{2.5}$

1213   enhancement. In all, the radiative feedback increased the cumulative rate of aerosols in the

1214   growth stage via promoting chemical formations, weakening vertical diffusions and/or

1215   enhancing regional transport by horizontal advection. For both episodes, the radiative

1216   feedback exerted small effect on the change rate of $PM_{2.5}$ concentration during the persistence

1217   stage and reinforced the decreasing rate of $PM_{2.5}$ in the dissipation stage.

1218

1219   **6 Conclusions**

1220   Several severe haze events occurred in the winter of 2014, with the most severe one on

1221   20–26 February. An online-coupled regional atmospheric chemistry/aerosol-climate model

1222   (RIEMS-Chem) was developed and utilized to investigate the mechanisms of haze formation

1223   and aerosol radiative feedback in the Beijing-Tianjin-Hebei (BTH) region. The heterogeneous

1224   chemical reactions were treated in the model and the measured size distribution and mixing

1225   state of aerosols in Beijing were used to constrain the model. Two numerical experiments,

1226   with and without aerosol effects were conducted to explore the aerosol radiative effects

1227   (AREs) and feedbacks on meteorological fields and aerosol distributions. Processes analysis

1228   technique was implemented in RIEMS-Chem to quantify the individual contributions from

1229   various physical and chemical processes to aerosol evolution and radiative feedback. Model

1230   performance was comprehensively evaluated by comparing with a variety of observations for

1231   meteorological variables, surface shortwave radiation, PBL heights, $PM_{2.5}$ and its chemical

1232   components, as well as aerosol optical properties in the BTH region. The comparisons

1233   demonstrated that RIEMS-Chem was able to represent the magnitudes and variations of the

1234   above variables reasonably well, in particular, improving the simulation of inorganic aerosols

1235   and AOD, which was often underpredicted in current on-line coupled models. It is

1236   encouraging that by considering the aerosol radiative effects, the model apparently improved

1237   predictions for meteorological variables, $PM_{2.5}$ and its chemical compositions and aerosol

1238   optical properties in the BTH region, suggesting the importance and necessity for developing

1239   chemistry-climate online coupled models in both air quality and climate research.

1240   During the study period, the meteorological conditions were characterized by weak

1241   southerly winds, high RH and low PBL height, which favored aerosol accumulation and haze

1242   formation in the BTH region. The average T2, WS10, RH2, PBL height and $PM_{2.5}$

1243   concentration from the FULL case were simulated to be 0.6 °C, 1.2 m s^{-1}, 67.0%, 698.4 m

1244   and 90.0 μg m^{-3}, respectively, over the BTH region during the study period.

1245   The distribution pattern of AOD generally resembled that of $PM_{2.5}$, with the domain

1246   mean value of 0.78 and the maximum up to 1.1 during the study period. It was noteworthy

1247   that the simulated SSA averaged over the BTH region and the study period was 0.91, which

1248   indicated the dominance of scattering aerosols. The domain and period average AREs at the

1249   surface, in the atmosphere and at the TOA were estimated to be -37 W m^{-2}, 19 W m^{-2} and -18

W m^{-2}, respectively, and they were enhanced to -57 W m^{-2}, 25 W m^{-2} and -32 W m^{-2} during the most severe haze episode (20–26 February). It was striking that the maximum hourly AREs at the surface and at TOA reached -384 W m^{-2} and -231 W m^{-2} around noon time in the vicinity of Shijiazhuang during the first haze episode. The magnitude of the model simulated AREs during the haze episode in this study agreed favorably with previous observational based estimates.

The aerosol radiative effects generally led to a reduction in surface air temperature in the entire domain with larger decrease in southern BTH (-1.2 °C to -2 °C), accompanied by an increase in RH2 (10% to 16%) and a decrease in PBL height (-240 m to -210 m). The changes in these meteorological variables were strengthened during the severe haze episode. Noticeably, PM$_{2.5}$ concentrations were consistently increased over the BTH region due to the aerosol feedback, with the maximum average increase exceeding 33 μg m^{-3} (33%) in southern Hebei and portions of Beijing and Tianjin during the study period, and the maximum hourly increase was up to 372 μg m^{-3} (186%) in the vicinity of Shijiazhuang during the severe haze episode. In terms of domain and period average, the feedback-induced changes were -1.4 °C for T2, -0.04 m s^{-1} for WS10, 8.7% for RH2, -3.3 m^2 s^{-1} for vertical diffusion coefficient, -160.0 m (-19%) for PBL height and 20.0 μg m^{-3} (29%) for PM$_{2.5}$ concentration. The magnitude of the above changes were enhanced during the severe haze episode, with the 7-day mean changes in T2, WS10, RH2, PBL height and PM$_{2.5}$ concentration being -1.8 °C, -0.5 m s^{-1}, 9.8%, -183.6 m (-31%) and 45.1 μg m^{-3} (39%), respectively, which demonstrated the significant aerosol radiative feedback on PM$_{2.5}$ accumulation and haze formation. The changes in sulfate and nitrate concentrations were larger than that in BC concentration because secondary aerosols were increased not only by weakened vertical diffusivity but also by enhanced chemical reactions caused by the feedback.

The magnitude of the feedback effect varied remarkably during haze evolution. The absolute change in PM$_{2.5}$ concentration caused by the feedback was largest in the persistence stage, followed by those in the growth stage and in the dissipating stage. In Beijing, the feedback-induced increases in PM$_{2.5}$ concentration were 55 μg m^{-3}, 84 μg m^{-3}, 40 μg m^{-3}, respectively, during the growth, persistence and dissipation stages of the severe haze episode.

PA method was applied to calculate the IPRs for quantifying the individual contributions

from physical and chemical processes to variations of $PM_{2.5}$ and its chemical components during haze episodes in Beijing. Two haze episodes were analyzed and compared to elucidate the mechanism of haze formation and evolution. For the first haze episode, the net IPR for $PM_{2.5}$ was 14.1 $\mu g\ m^{-3}\ h^{-1}$ in the growth stage, in which emissions, chemical processes and physical processes contributed 29.8 $\mu g\ m^{-3}\ h^{-1}$, 33.5 $\mu g\ m^{-3}\ h^{-1}$ and -49.2 $\mu g\ m^{-3}\ h^{-1}$, respectively, which indicated a remarkable $PM_{2.5}$ increase contributed by chemical processes in this stage. The most influential processes for $PM_{2.5}$ loss and production were vertical diffusion and thermodynamic processes, respectively. Compared with the clean stage, the losses by vertical diffusion and dry deposition reduced largely, and the production by chemical processes increased, both leading to an evident increase in surface $PM_{2.5}$ concentrations in the growth stage. In the persistence stage, the production and loss of $PM_{2.5}$ were almost equal, resulting in an approximately zero IPR in this stage. In the dissipation stage, the loss of $PM_{2.5}$ by vertical diffusion and dry deposition increased greatly, leading to a net IPR rate of -34.8 $\mu g\ m^{-3}\ h^{-1}$, which meant a substantial decrease in $PM_{2.5}$ concentration.

For the second haze episode, the net IPR for $PM_{2.5}$ was 13.0 $\mu g\ m^{-3}\ h^{-1}$ in the growth stage, in which emissions, chemical processes and physical processes contributed 29.8 $\mu g\ m^{-3}\ h^{-1}$, 23.9 $\mu g\ m^{-3}\ h^{-1}$ and -40.8 $\mu g\ m^{-3}\ h^{-1}$, respectively. It was noteworthy that the contribution of horizontal advection to $PM_{2.5}$ was of a similar magnitude to the contributions from local emissions and chemical processes, with the mean IPR of 22.4 $\mu g\ m^{-3}\ h^{-1}$, which indicated the important contribution of regional transport to haze formation in Beijing. Process analysis for the changes in $PM_{2.5}$ components during haze evolution was also conducted.

The contribution of each physical and chemical process to the feedback-induced changes in $PM_{2.5}$ and its major components were explored and quantified. For the first haze episode, the fast increase in $PM_{2.5}$ (ΔIPR of 9.5 $\mu g\ m^{-3}\ h^{-1}$) due to aerosol feedback in the growth stage was mainly attributed to the changes in vertical movements (VDIF and VADV) and chemical processes, but the increased outflow via horizontal advection (HADV) partly offset the increased $PM_{2.5}$ due to vertical movements, which caused a larger contribution to the $PM_{2.5}$ increase from chemical processes (ΔIPR of 7.27 $\mu g\ m^{-3}\ h^{-1}$) than that from physical processes (ΔIPR 2.23 $\mu g\ m^{-3}\ h^{-1}$). However, during the second haze episode, the feedback-induced $PM_{2.5}$ increase (ΔIPR of 2.4 $\mu g\ m^{-3}\ h^{-1}$) in the growth stage was mainly contributed by

physical processes (ΔIPR of 1.40 μg m^{-3} h^{-1}) rather than that by chemical processes (ΔIPR of 1.0 μg m^{-3} h^{-1}), and among physical processes, the PM$_{2.5}$ increase was mainly attributed to the increased horizontal advection (ΔIPR of 10.2 μg m^{-3} h^{-1}). In general, in the growth stage of haze episodes, the feedback increased the accumulation rate of aerosols mainly through enhancing chemical formations, weakening vertical diffusions and/or enhancing regional transport by advections. The feedback-induced changes in the change rate of PM$_{2.5}$ concentration were small during the persistence stage, and the feedback enhanced the removal rate of PM$_{2.5}$ in the dissipation stage mainly through increasing vertical diffusion and/or vertical advection.

The results from this study demonstrated a significant impact of aerosol radiative feedback on meteorology, chemistry, aerosol distribution and evolution during winter haze events in the BTH region. The mechanism and processes through which the feedback affected haze formation and evolution were elucidated and quantified. This study is still subject to some uncertainties: 1.) An internal mixing was assumed for aerosol mixing in this study, but the mixing state of aerosols is always changing, while this assumption is generally realistic for haze days, it may overestimate the feedback effect for clean days. 2.) A typical size distribution measured during haze days was used, whereas the size of aerosol internal mixture could change to some extent with aging processes. These uncertainties require further development of model treatment for evolution of aerosol mixing state and size distribution, which is poorly represented in current online coupled models. 3.) Direct aerosol radiative effect dominated the feedback effect in this study, so more cases in different regions and seasons, when indirect effect could be more important are needed to elucidate the complete feedback mechanism at different spatial and temporal scales. 4.) Finer model grid resolution is expected to be applied to look into details of the feedback effect at urban scale along with finer emission inventory (Tao et al., 2020), vertical observations (Wilcox et al., 2016; Wang et al., 2018) and higher computational efficiency when available in the future. Finally, this study pointed out the significance and necessity of developing online coupled model for exploring chemistry/aerosol-weather/climate interactions and for improving meteorological and chemical predictions in both air quality and climate research in the future.

Author Contributions

ZH designed the study, JL performed the model simulation, JL and ZH processed and analyzed the modeling data, ZH and JL wrote the paper, JL and ZX contributed to the model development, YW provided and analyzed the chemical observation data, XX provided the meteorological sounding and aerosol optical observation data, JL and LL processed and analyzed the observational data, RZ synthesized and analyzed the observation.

Data availability.

The observational data can be accessed through contacting the corresponding authors.

Competing interests.

The authors declare that they have no conflict of interests.

Special issue statement.

This article is part of the special issue "Regional assessment of air pollution and climate change over East and Southeast Asia: results from MICS-Asia Phase III". It is not associated with a conference.

Acknowledgement.

This study was supported by the National Natural Science Foundation of China (no. 91644217), the National Key R&D Program of China (2019YFA0606802) and the Jiangsu Collaborative Innovation Center for Climate Change.

References

Albrecht, B.: Aerosols, cloud microphysics, and fractional cloudiness, Science, 245, 1227, https://doi.org/10.1126/science.245.4923.1227, 1989.

An, Z., Huang, R., Zhang, R., Tie, X., Li, G., Cao, J., Zhou, W., Shi, Z., Han, Y., Gu, Z., and Ji, Y.: Severe haze in northern China: A synergy of anthropogenic emissions and atmospheric processes, P. Natl. Acad. Sci. USA, 116,18, 8657–8666, 2019.

Baklanov, A., Schlunzen, K., Suppan, P., Baldasano, J., Brunner, D., Aksoyoglu, S., Carmichael, G., Douros, J., Flemming, J., Forkel, R., Galmarini, S., Gauss, M., Grell, G., Hirtl, M., Joffre, S., Jorba, O., Kaas, E., Kaasik, M., Kallos, G., Kong, X., Korsholm, U., Kurganskiy, A., Kushta, J., Lohmann, U., Mahura, A., Manders-Groot, A., Murizi, A., Moussiopoulos, N., Rao, S.T., Savage, N., Seigneur, C., Sokhi, R.S., Solazzo, E., Solomos, S., Sorenson, B., Tsegas, G., Vignati, E., Vogel, B., and Zhang, Y.: Online coupled regional meteorology chemistry models in Europe: current status and prospects, Atmos. Chem. Phys., 14, 317-398, doi:10.5194/acp-14-317-2014, 2014.

Beheng, K. D.: A parameterization of warm cloud microphysical conversion processes, Atmos. Res., 33, 193–206, 1994.

Cai, W., Li, K., Liao, H., Wang, H., and Wu, L.: Weather conditions conducive to Beijing severe haze more frequent under climate change, Nature Clim. Change, 7, 257–262, doi: 10.1038/nclimate3249, 2017.

Carslaw, K. S., Boucher, O., Spracklen, D. V., Mann, G. W., Rae, J. G. L., Woodward, S., and Kulmala, M.: A review of natural aerosol interactions and feedbacks within the Earth system, Atmos. Chem. Phys., 10, 1701–1737, doi:10.5194/acp-10-1701-2010, 2010.

Chan, C. and Yao, X.: Air pollution in megacities in China, Atmos. Environ., 42, 1-42, 2008.

Che H., Xia, X., Zhu, J., Li, Z., Dubovik, O., Holben, B., Goloub, P., Chen, H., Estelles, V., Cuevas-Agulló, E., Blarel, L., Wang, H., Zhao, H., Zhang, X., Wang, Y., Sun, J., Tao, R., Zhang, X., and Shi, G.: Column aerosol optical properties and aerosol radiative forcing during a serious haze-fog month over North China Plain in 2013 based on ground-based sunphotometer measurements, Atmos. Chem. Phys., 14, 2125–2138, doi:10.5194/acp-14-2125-2014, 2014.

Chen, L., Zhu, J., Liao, H., Gao, Y., Qiu, Y., Zhang, M. G., Liu, Z. R., Li, N., and Wang, Y. S.: Assessing the formation and evolution mechanisms of severe haze pollution in the Beijing–Tianjin–Hebei region using process analysis, Atmos. Chem. Phys., 19, 10845–10864, 2019.

Cheng, Y., Zheng, G., Wei, C., Mu, Q., Zheng, Bo., Wang, Z., Gao, M., Zhang, Q., He, K., Carmichael, G., Pösch, U., and Su, H.: Reactive nitrogen chemistry in aerosol water as a source of sulfate during haze events in China, Sci. Adv., 2, e1601530, 2016.

Dawson, J. P., Adams, P. J., and Pandis, S. N.: Sensitivity of $PM_{2.5}$ to climate in the Eastern US: a modeling case study, Atmos. Chem. Phys., 7, 4295–4309, 2007.

Dickinson, R.E., Henderson-Sellers, A., and Kennedy, P.J.: Biosphere-Atmosphere Transfer Scheme (BATS) Version 1e as coupled to NCAR Community Climate Model, NCAR Technical Note, NCAR/TN-387+STR, p.72, 1993.

Ding, A., Huang, X., Nie, W., Sun, J., Kerminen, V. M., Petäjä, T., Su, H., Cheng, Y., Yang, X., Wang, M., Chi, X., Wang, J., Virkkula, A., Guo, W., Yuan, J., Wang, S., Zhang, R., Wu, Y., Song, Y., Zhu, T., Zilitinkevich, S., Kulmala, M., and Fu, C.: Enhanced haze pollution by black carbon in megacities in China, Geophys. Res. Lett., 43, 2873-2879, 10.1002/2016gl067745, 2016.

Emmons, L. K., Walters, S., Hess, P. G., Lamarque, J. F., Pfister, G. G., Fillmore, D., Granier, C., Guenther, A., Kinnison, D., Laepple, T., Orlando, J., Tie, X., Tyndall, G., Wiedinmyer, C., Baughcum, S. L., and Kloster, S.: Description and evaluation of the Model for Ozone and Related chemical Tracers, version 4 (MOZART-4), Geosci. Model. Dev., 3, 43-67, doi:10.5194/gmd-3-43-2010, 2010.

Forkel, R., Werhahn, J., Hansen, A. B., McKeen, S., Peckham, S., Grell, G., and Suppan, P.: Effect of aerosol–radiation feedback on regional air quality – a case study with WRF/Chem, Atmos. Environ., 53, 202–211, 2012.

Fountoukis, C. and Nenes, A.: ISORROPIA II: a computationally efficient thermodynamic equilibrium model for $K^+–Ca^{2+}–Mg^{2+}–NH_4^+–Na^+–SO_4^{2-}–NO_3^-–Cl^-–H_2O$ aerosols, Atmos. Chem. Phys., 7, 4639-4659, 2007.

Fu, C. B., Wang, S. Y., Xiong, Z., Gutowski, W. J., Lee, D., Mcgregor, J. L., Sato, Y., Kato,

H., Kim, J., and Suh, M.: Regional climate model intercomparison project for Asia, Bull. Amer. Meteor. Soc., 86, 257-266, 2005.

Fu, H. and Chen, J.: Formation, features and controlling strategies of severe haze-fog pollutions in China, Sci. Total. Environ., 578, 121–138, 2017.

Gao, M., Carmichael, G. R., Wang, Y., Saide, P. E., Yu, M., Xin, J., Liu, Z., and Wang, Z.: Modeling study of the 2010 regional haze event in the North China Plain, Atmos. Chem. Phys., 16, 1673-1691, 10.5194/acp-16-1673-2016, 2016.

Gao, M., Han, Z., Liu, Z., Li, M., Xin, J., Tao, Z., Li, J., Kang, J., Huang, K., Dong, X., Zhuang, B., Li, S., Ge, B., Wu, Q., Cheng, Y., Wang, Y., Lee, H., Kim, C., Fu, J. S., Wang, T., Chin, M., Woo, J., Zhang, Q., Wang, Z., and Carmichael G. R.: Air Quality and Climate Change, Topic 3 of the Model Inter-Comparison Study for Asia Phase III (MICS-Asia III), Part I: overview and model evaluation, Atmos. Chem. Phys., 18, 4859–4884, https://doi.org/10.5194/acp-18-4859-2018, 2018.

Gao, M., Han, Z. W., Tao, Z. N., Li, J. W., Kang, J.-E., Huang, K., Dong, X. Y., Zhuang, B. L., Li, S., Ge, B. Z., Wu, Q. Z., Lee, H.-J., Kim, C. H., Fu, J. S., Wang, T. J., Chin, M., Li, M., Woo, J.-H., Zhang, Q., Cheng, Y. F., Wang, Z. F., and Carmichael, G. R.: Air quality and climate change, Topic 3 of the Model Inter-Comparison Study for Asia Phase III (MICS-Asia III) – Part 2: aerosol radiative effects and aerosol feedbacks. Atmospheric Chemistry and Physics, 20, 1147–1161, 2020.

Gao, Y., Zhang, M., Liu, Z., Wang, L., Wang, P., Xia, X., Tao, M., and Zhu, L.: Modeling the feedback between aerosol and meteorological variables in the atmospheric boundary layer during a severe fog–haze event over the North China Plain, Atmos. Chem. Phys., 15, 4279-4295, 10.5194/acp-15-4279-2015, 2015.

Gery, M.W., Whitten, G.Z., Killus, J.P., and Dodge, M.C.: A photochemical kinetics mechanism for urban and regional scale computer modeling, J. Geophys. Res., 94, 12925-12956, 1989.

Ghan, S. and Zaveri R.A.: Parameterization of optical properties for hydrated internally mixed aerosol, J. Geophys. Res., 112, D10201, doi:10.1029/2006JD007927, 2007.

Giglio, L., Randerson, J. T., and van der Werf, G. R.: Analysis of daily, monthly, and annual burned area using the fourth generation Global Fire Emissions Database (GFED4), J. Geophys. Res.: Biogeosciences, doi:10.1002/jgrg.20042, 2013.

Grell, G. A.: Prognostic evaluation of assumptions used by cumulus parameterizations, Mon. Weather. Rev., 121, 764-787, 1993.

Guo, S., Hu, M., Zamora, M. L., Peng, J., Shang, D., Zheng, J., Du, Z., Wu, Z., Shao, M., Zeng, L., Molina, M. J., and Zhang, R. : Elucidating severe urban haze formation in China, P. Natl. Acad. Sci. USA., 111, 17373–17378, https://doi.org/10.1073/pnas.1419604111, 2014.

Han, X., Zhang, M. G., Han, Z. W., Xin, J. Y., and Liu, X. H.: Simulation of aerosol direct radiative forcing with RAMS-CMAQ in East Asia, Atmos. Environ., 45, 6576-6592, 2011a.

Han, Z. W., Ueda, H., Matsuda, K., Zhang, R. J., Arao, K., Kanai, Y., and Hasome, H.: Model study on particle size segregation and deposition during Asian dust events in March 2002, J. Geophys. Res., 109, D19205, doi: 10.1029/2004jd004920, 2004.

Han, Z. W.: Direct radiative effect of aerosols over East Asia with a Regional coupled

Climate/Chemistry model, Meteorol. Z., Vol. 19, No. 3, 287-298, 2010.

Han, Z. W., Xiong, Z., and Li, J. W.: Direct climatic effect of aerosols and interdecadal variations over East Asia investigated by a regional climate/chemistry model, Atmospheric and Oceanic Science Letters, 4(6), 299-303, 2011b.

Han, Z. W., Li, J. W., Xia, X. A., and Zhang, R. J.: Investigation of direct radiative effects of aerosols in dust storm season over East Asia with an online coupled regional climate-chemistry-aerosol model, Atmos. Environ., 54, 688-699, 2012.

Han, Z. W., Li, J. W., Guo, W. D., Xiong, Z., and Zhang, W.: A study of dust radiative feedback on dust cycle and meteorology over East Asia by a coupled regional climate-chemistry-aerosol model, Atmos. Environ., 68, 54-63, 2013.

Han, Z. W., Li, J. W., Yao, X. H., and Tan, S. C.: A regional model study of the characteristics and indirect effects of marine primary organic aerosol in springtime over East Asia, Atmos. Environ., 197, 22–35, 2019.

Hegg D. A.: Cloud condensation nucleus-sulfate mass relationship and cloud albedo. J. Geophys. Res. Atmos., 99, D12, 25903-25907, 1994.

Hess, M., Koepke, P., and Schuit, I.: Optical properties of aerosols and clouds: the software package OPAC, Bull. Amer. Meteor. Soc., 79, 831-844 ,1998.

Heo, B.-H., Jacoby-Koaly, S., Kim, K.-E., Campistron, B., Benech, B., and Jung, E.-S.: Use of the Doppler Spectral Width to Improve the Estimation of the Convective Boundary Layer Height from UHF Wind Profiler Observations, J. Atmos. Ocean. Technol., 20, 408-424, 2003.

Hong, S. and Pan, H.: Nonlocal boundary layer vertical diffusion in a medium-range forecast model, Mon. Weather Rev., 124, 2322–2339, 1996.

Huang, R. J., Zhang, Y., Bozzetti, C., Ho, K. F., Cao, J. J., Han, Y., Daellenbach, K. R., Slowik, J. G., Platt, S. M., Canonaco, F., Zotter, P., Wolf, R., Pieber, S. M., Bruns, E. A., Crippa, M., Ciarelli, G., Piazzalunga, A., Schwikowski, M., Abbaszade, G., Schnelle-Kreis, J., Zimmermann, R., An, Z., Szidat, S., Baltensperger, U., El Haddad, I., and Prevot, A. S.: High secondary aerosol contribution to particulate pollution during haze events in China, Nature, 514, 218-222, 10.1038/nature13774, 2014.

Huang, X., Wang, Z. L., Ding, A. J.: Impact of Aerosol-PBL Interaction on Haze Pollution: Multiyear Observational Evidences in North China, Geophys. Res. Lett., 45, 8596-8603, 2018.

Isaksen I.S.A., Granier, C., Myhre, G., Berntsen, T.K., Dalsøren, S.B., Gauss, M., Klimont, Z., Benestad, R., Bousquet, P., Collins, W., Cox, T., Eyring, V., Fowler, D., Fuzzi, S., Jo¨ckel, P., Laj, P., Lohmann, U., Maione, M., Monks, P., Prevot, A.S.H., Raes, F., Richter, A., Rognerud, B., Schulz, M., Shindell, D., Stevenson, D.S., Storelvmo, T., Wang, W.-C., van Weele, M., Wild, M., and Wuebbles, D.: Atmospheric composition change: Climate–Chemistry interactions, Atmos. Environ., 43, 5138–5192, 2009.

Jing, J., Wu, Y., Tao, J., Che, H.Z, Xia, X., Zhang, X., Yan, P., Zhao, D.M., and Zhang, L.M.: Observation and analysis of near-surface atmospheric aerosol optical properties in urban Beijing, Particuology, 18, 144-154, 2015.

Kajino, M., Ueda, H., Han, Z. W., Kudo, R., Inomata, Y., Kaku, H.: Synergy between air pollution and urban meteorological changes through aerosol-radiation-diffusion feedback—A case study of Beijing in January 2013, Atmos. Environ., 171, 98-110,

2017.

Keihl, J.T., Hack, J.J., Bonan, G.B., Boville, B.A., Briegleb, B.P., Williamson, D.L., and Rasch, P.J.: Description of the NCAR Community Climate Model (CCM3), NCAR Technical Note, NCAR/TN-420+STR, p.152 , 1996.

Lee-Taylor, J., Madronich, S.: Climatology of UV-A, UV-B, and Erythemal Radiation at the Earth's Surface, 1979-2000, NCAR Technical Note, NCAR/TN-474+STR, pp 1-52. 2007.

Li, G.H., Bei, N.F., Cao, J.J., Huang, R.J., Wu, J.R., Feng, T., Wang, Y.C., Liu, S.X., Zhang, Q., Tie, X.X., and Molina, L.T.: A possible pathway for rapid growth of sulfate during haze days in China, Atmos. Chem. Phys., 17, 3301-3316, 2017c.

Li, J., Chen, X.S., Wang, Z.F., Du, H.Y., Yang, W.Y., Sun, Y.L., Hu, B., Li, J.J., Wang, W., Wang, T., Fu, P.Q., and Huang, H.L.: Radiative and heterogeneous chemical effects of aerosols on ozone and inorganic aerosols over East Asia, Sci. Total. Environ., 622–623, 1327–1342 , 2018b.

Li, J. W. and Han, Z. W.: A modeling study of the impact of heterogeneous reactions on mineral aerosol surfaces on tropospheric chemistry over East Asia, Particuology, 8, 433-441, 2010.

Li, J. W., Han, Z. W., and Zhang, R. J.: Influence of aerosol hygroscopic growth parameterization on aerosol optical depth and direct radiative forcing over East Asia, Atmos. Res., 140-141, 14-27, 2014.

Li, J. W. and Han, Z. W.: A modeling study of severe winter haze events in Beijing and its neighboring regions, Atmos. Res., 170, 87–97, 2016a.

Li, J. W. and Han, Z. W.: Aerosol vertical distribution over east China from RIEMS-Chem simulation in comparison with CALIPSO measurements, Atmos. Environ., 143, 177-189, 2016b.

Li, J. W. and Han, Z. W.: Seasonal variation of nitrate concentration and its direct radiative forcing over East Asia, Atmosphere, 7(8), 105, 2016c.

Li, J. W., Han, Z. W., and Yao, X. H.: A modeling study of the influence of sea salt on inorganic aerosol concentration, size distribution, and deposition in the western Pacific Ocean, Atmos. Environ., 188, 157-173, 2018a.

Li, J. W., Han, Z. W., Yao, X. H., Xie, Z. X., and Tan, S. C.: The distributions and direct radiative effects of marine aerosols over East Asia in springtime, Sci. Total. Environ., 651, 1913–1925, 2019b.

Li, M., Zhang, Q., Kurokawa, J.-I., Woo, J.-H., He, K., Lu, Z., Ohara, T., Song, Y., Streets, D. G., Carmichael, G. R., Cheng, Y., Hong, C., Huo, H., Jiang, X., Kang, S., Liu, F., Su, H., and Zheng, B.: MIX: a mosaic Asian anthropogenic emission inventory under the international collaboration framework of the MICS-Asia and HTAP, Atmos. Chem. Phys., 17, 935-963, 10.5194/acp-17-935-2017, 2017a.

Li, X., Wu, J., Elser, M., Tong, S., Liu, S., Li, X., Liu, L., Cao, J., Zhou, J., El-Haddad, I., Huang, R., Ge, M., Tie, X., André S. H. Prévôt, and Li, G.: Wintertime secondary organic aerosol formation in Beijing–Tianjin–Hebei (BTH): contributions of HONO sources and heterogeneous reactions, Atmos. Chem. Phys., 19, 2343–2359, https://doi.org/10.5194/acp-19-2343-2019, 2019a.

Li, Z., Guo, J., Ding, A., Liao, H., Liu, J., Sun, Y., Wang, T., Xue, H., Zhang, H., and Zhu, B.:

Aerosol and boundary-layer interactions and impact on air quality, Natl. Sci. Rev., 4, 810–833, 10.1093/nsr/nwx117, 2017b.

Liu, X. H. and Wang, J.: How important is organic aerosol hygroscopicity to aerosol indirect forcing? Environ. Res. Lett., 5(4), 044010, http://iopscience.iop.org/1748-9326/5/4/044010, 2010a.

Liu, X. H., Zhang, Y., Xing, J., Zhang, Q., Wang, K., Streets, D., Jang, C., Wang, W.-X., and Hao, J.-M.: Understanding of regional air pollution over China using CMAQ, part II. Process analysis and sensitivity of ozone and particulate matter to precursor emissions, Atmos. Environ., 44, 3719-3727, 2010b.

Ma, N., Zhao, C. S., Müller, T., Cheng, Y. F., Liu, P. F., Deng, Z. Z., Xu, W. Y., Ran, L., Nekat, B., van Pinxteren, D., Gnauk, T., Müller, K., Herrmann, H., Yan, P., Zhou, X.J., and Wiedensohler, A.: A new method to determine the mixing state of light absorbing carbonaceous using the measured aerosol optical properties and number size distributions, Atmos. Chem. Phys., 12, 2381–2397, 2012.

Ma, Q. X., Wu, Y. F., Zhang, D. Z., Wang, X. J., Xia, Y. J., Liu, X. Y., Tian, P., Han, Z. W., Xia, X. A., Wang, Y., and Zhang, R. J.: Roles of regional transport and heterogeneous reactions in the $PM_{2.5}$ increase during winter haze episodes in Beijing, Sci. Total. Environ., 599–600, 246–253, 2017.

Martin, G. M., Johnson, D. W., and Spice, A.: The Measurements and Parameterization of Effective Radius of Droplets in Warm Stratocumulus Clouds, J. Atmos. Sci., 51, 1823–1842, 1994.

NOAA/NCEP.: NCEP FNL Operational Model Global Tropospheric Analyses, continuing from July 1999. Research Data Archive at the National Center for Atmospheric Research, Computational and Information Systems Laboratory, Dataset. https://doi.org/10.5065/D6M043C6, Last accessed, 12 April 2019, 2000.

Odum, J.R., Jungkamp, T.P.W., Griffin, R.J., Flagan, R.C., and Seinfeld, J.H.: The atmospheric aerosol-forming potential of whole gasoline vapor, Science. 276, 96–99, 1997.

Petters, M.D. and Kreidenweis, S.M.: A single parameter representation of hygroscopic growth and cloud condensation nucleus activity, Atmos. Chem. Phys., 7, 1961-1971, 2007.

Qiu, Y., Liao, H., Zhang, R., and Hu, J.: Simulated impacts of direct radiative effects of scattering and absorbing aerosols on surface layer aerosol concentrations in China during a heavily polluted event in February 2014, J. Geophys. Res. Atmos., 122, 5955-5975, 10.1002/2016jd026309, 2017.

Ramanathan, V., Crutzen, P. J., Kiehl, J. T., and Rosenfeld, D.: Aerosols, climate, and the hydrological cycle, Science, 294, 2119-2124, 10.1126/science.1064034, 2001.

Riemer, N., West, M., Zaveri, R., and Easter, R.: Estimating black carbon aging time-scales with a particle-resolved aerosol model, J. Aerosol Sci., 41, 143-158, 2010.

Song, Z.J., Fu, D.S., Zhang, X.L., Wu, Y.F., Xia, X.A., He, J.X., Han, X.L., Zhang, R.J., and Che, H.Z.: Diurnal and seasonal variability of $PM_{2.5}$ and AOD in North China plain: Comparison of MERRA-2 products and ground measurements, Atmos. Environ., 191, 70-78, 2018.

Sun, Y., Jiang, Q., Wang, Z., Fu, P., Li, J., Yang, T., and Yin, Y.: Investigation of the Sources

and Evolution Processes of Severe Haze Pollution in Beijing in January 2013, J. Geophys. Res., 119, 4380–4398, 2014.

Tao, Z. N., Chin, M., Gao, M., Kucsera, T., Kim, D.-C., Bian, H. S., Kurokawa, J.-I., Wang, Y. S., Liu, Z. R., Carmichael, G. R., Wang, Z. F., and Akimoto, H.: Evaluation of NU-WRF model performance on air quality simulation under various model resolutions – an investigation within the framework of MICS-Asia Phase III. Atmos. Chem. Phys., 20, 2319–2339, 2020.

Twomey, S.: Pollution and the planetary albedo, Atmos. Environ., 8, 1251–1256, 1974.

Wang, J., Wang, S., Jiang, J., Ding, A., Zheng, M., Zhao, B., Wong, D. C., Zhou, W., Zheng, G., and Wang, L.: Impact of aerosol-meteorology interactions on fine particle pollution during China's severe haze episode in January 2013, Environ. Res. Lett., 9, 094002, https://doi.org/10.1088/1748-9326/9/9/094002, 2014b.

Wang, S. Y., Fu, C. B., Wei, H. L., Qian, Y., Xiong, Z., Feng, J.M., Zhao, D. M., Dan, L., Han, Z.W., Su, B.K., Zhao, M., Zhang, Y.C., Tang, J.P., Liu, H.N., Wu, J., Zeng, X.M., Chen, M., and Wang, L.Z.: Regional integrated environmental modeling system: development and application, Climate Change, 129, 499-510, 2015.

Wang, Y., Bao, S., Wang, S., Hu, Y., Shi, X., Wang, J., Zhao, B., Jiang, J., Zheng, M., Wu, M., Russell, A. G., Wang, Y., and Hao, J.: Local and regional contributions to fine particulate matter in Beijing during heavy haze episodes, Sci. Total. Environ., 580, 283-296, 10.1016/j.scitotenv.2016.12.127, 2017.

Wang, Z. L., Huang, X., Ding, A. J.: Dome effect of black carbon and its key influencing factors: a one-dimensional modelling study, Atmos. Chem. Phys., 18, 2821–2834, 2018.

Wang, Z., Li, J., Wang, Z., Yang, W., Tang, X., Ge, B., Yan, P., Zhu, L., Chen, X., Chen, H., Wand, W., Li, J., Liu, B., Wang, X., Wand, W., Zhao, Y., Lu, N., and Su, D.: Modeling study of regional severe hazes over mid-eastern China in January 2013 and its implications on pollution prevention and control, Sci. China. Earth. Sci., 57, 3-13, 10.1007/s11430-013-4793-0, 2014a.

Westervelt, D. M., Moore, R. H., Nenes, A. and Adams, P.J.: Effect of primary organic sea spray emissions on cloud condensation nuclei concentrations, Atmos. Chem. Phys., 12, 89–101, 2012.

Wilcox, E. M., Thomas, R. M., Praveen, P. S., Pistone, K., Bender, F. A., and Ramanathan, V.: Black carbon solar absorption suppresses turbulence in the atmospheric boundary layer. Proc. Natl. Acad. Sci. USA, 113(42), 11794–11799, 2016.

Wu, J., Bei, N., Hu, B., Liu, S., Zhou, M., Wang, Q., Li, X., Liu, L., Feng, T., Liu, Z., Wang, Y., Cao, J., Tie, X., Wang J., Molina, L.T., and Li, G.: Aerosol–radiation feedback deteriorates the wintertime haze in the North China Plain, Atmos. Chem. Phys., 19, 8703–8719, https://doi.org/10.5194/acp-19-8703-2019, 2019.

Wu, Y. F., Zhang, R. J., Tian, P., Tao, J., Hsu, S.-C., Yan, P., Wang, Q. Y., Cao, J. J., Zhang, X. L., and Xia, X. A.: Effect of ambient humidity on the light absorption amplification of black carbon in Beijing during January 2013, Atmos. Environ., 124, 217-223 , 2016.

Xiong, Z., Fu, C. B., and Yan, X. D.: Regional Integrated environmental model system and its simulation of East Asia summer monsoon, Chinese. Sci. Bull., 54(22), 4253-4261, 2009.

Yu, S., Mathur, R., Schere, K., Kang, D., Plein, J., Young, J., Tong, D., Pouliot, G., Mckeen, S.A., and Rao, S. T.: Evaluation of real-time $PM_{2.5}$ forecasts and process analysis for

PM$_{2.5}$ formation over the eastern United States using the Eta-CMAQ forecast model during the 2004 ICARTT study, J. Geophys. Res., 113, D06204, doi: 10.1029/2007JD009226, 2008.

Zhang, B., Wang, Y., and Hao, J.: Simulating aerosol–radiation–cloud feedbacks on meteorology and air quality over eastern China under severe haze conditions in winter, Atmos. Chem. Phys., 15, 2387-2404, 10.5194/acp-15-2387-2015, 2015.

Zhang, X. Y., Wang, Y. Q., Niu, T., Zhang, X. C., Gong, S. L., Zhang, Y. M., and Sun, J. Y.: Atmospheric aerosol compositions in China: spatial/temporal variability, chemical signature, regional haze distribution and comparisons with global aerosols, Atmos. Chem. Phys., 12, 779–799, https://doi.org/10.5194/acp-12-779-2012, 2012.

Zhang, X., Zhong, J., Wang, J., Wang, Y., and Liu, Y.: The interdecadal worsening of weather conditions affecting aerosol pollution in the Beijing area in relation to climate warming, Atmos. Chem. Phys., 18, 5991–5999, https://doi.org/10.5194/acp-18-5991-2018, 2018a.

Zhang, X., Zhang, Q., Hong, C., Zheng, Y., Geng, G., Tong, D., Zhang, Y. and Zhang, X.: Enhancement of PM$_{2.5}$ Concentrations by Aerosol-Meteorology Interactions Over China, J. Geophys. Res. Atmos., 123, https://doi.org/10.1002/2017JD027524, 2018b.

Zhang, Y.: Online coupled meteorology and chemistry models: history, current status, and outlook, Atmos. Chem. Phys., 8, 2895-2932, 2008.

Zhang, Y., Wen, X.-Y., Wang, K., Vijayaraghavan, K., and Jacobson, M. Z.: Probing into regional O$_3$ and PM pollution in the U.S., PartII. An examination of formation mechanisms through a process analysis technique and sensitivity study, J. Geophys. Res.,114 (D22305), doi:10.1029/2009JD011900, 2009.

Zhang, Y., Wen, X. Y., and Jang, C. J.: Simulating chemistry-aerosol-cloud-radiation-climate feedbacks over the continental U.S. using the online-coupled weather research forecasting model with chemistry (WRF/Chem), Atmos. Environ., 44, 3568–3582, 2010.

Zhao, B., Liou, K. N., Gu, Y., Li, Q., Jiang, J. H., Su, H., He, C., Tseng, H. R., Wang, S., Liu, R., Qi, L., Lee, W. L., and Hao, J.: Enhanced PM$_{2.5}$ pollution in China due to aerosol-cloud interactions, Sci. Rep., 7, 4453, 10.1038/s41598-017-04096-8, 2017.

Zhao, D. M.: Performance of Regional Integrated Environment Modeling System (RIEMS) in precipitation simulations over East Asia, Clim. Dynam. 40, 1767-1787, 2013.

Zhao, P., Dong, F., Yang, Y., He, D., Zhao, X., and Zhang, W.: Characteristics of carbonaceous aerosol in the region of Beijing, Tianjin, and Hebei, China, Atmos. Environ., 71, 389–398, 2013.

Zheng, B., Zhang, Q., Zhang, Y., He, K. B., Wang, K., Zheng, G. J., Duan, F. K., Ma, Y. L., and Kimoto, T.: Heterogeneous chemistry: a mechanism missing in current models to explain secondary inorganic aerosol formation during the January 2013 haze episode in North China, Atmos. Chem. Phys., 15, 2031–2049, doi:10.5194/acp-15-2031-2015, 2015.

Zhong, J., Zhang, X., Dong, Y., Wang, Y., Liu, C., Wang, J., Zhang, Y., and Che, H.: Feedback effects of boundary-layer meteorological factors on cumulative explosive growth of PM$_{2.5}$ during winter heavy pollution episodes in Beijing from 2013 to 2016, Atmos. Chem. Phys., 18, 247–258, https://doi.org/10.5194/acp-18-247-2018, 2018a.

Zhong, J., Zhang, X., Wang, Y., Liu, C., and Dong, Y.: Heavy aerosol pollution episodes in winter Beijing enhanced by radiative cooling effects of aerosols, Atmos. Res., 209, 59–

1685   64, https://doi.org/10.1016/j.atmosres.2018.03.011, 2018b.

1686   Zhuang, B. L., Li, S., Wang, T. J., Deng, J. J., Xie, M., Yin, C. Q., and Zhu, J. L.: Direct
1687   radiative forcing and climate effects of anthropogenic aerosols with different mixing
1688   states over China, Atmos. Environ., 79, 349-361, 2013.

1689

1690

1691
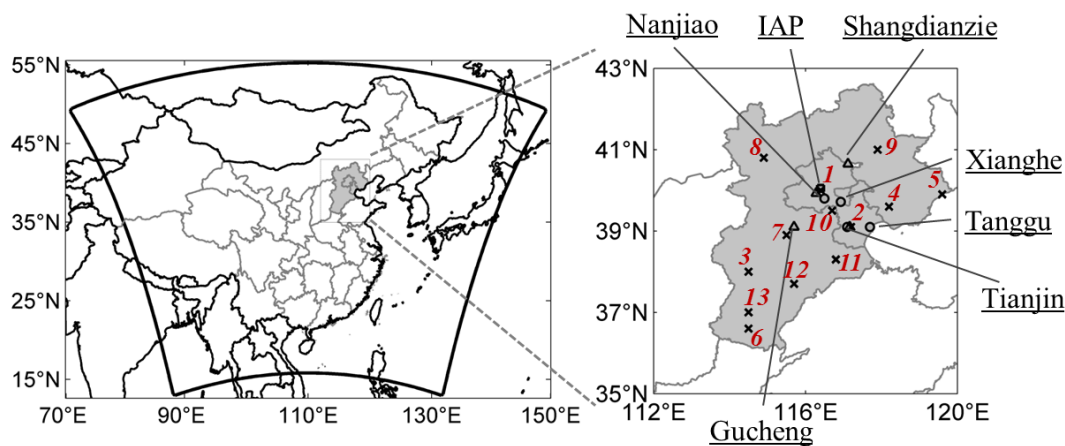
1692

Figure 1. The model study domain. The shaded areas indicate the Beijing-Tianjin-Hebei (BTH) region. Markers are observation sites (square: IAP, observations of $PM_{2.5}$, its chemical components, aerosol extinction coefficient (EXT) and aerosol absorption coefficient (ABS); circles: observations of meteorological variables; triangles: aerosol optical depth. The Xianghe site provides meteorological soundings and hourly surface shortwave radiation (SWDOWN) measurements; the Tianjin site provides both meteorological variables and AOD). Hourly O_3, SO_2, NO_2 and $PM_{2.5}$ measurements at 13 cities from the CNEMC (China National Environmental Monitoring Center, http://www.cnemc.cn/) are labeled by crosses with numbers (1-Beijing, 2-Tianjin, 3-Shijiazhuang, 4-Tangshan, 5-Qinhuangdao, 6-Handan, 7-Baoding, 8-Zhangjiakou, 9-Chengde, 10-Langfang, 11-Cangzhou, 12-Hengshui and 13-Xingtai).

1704
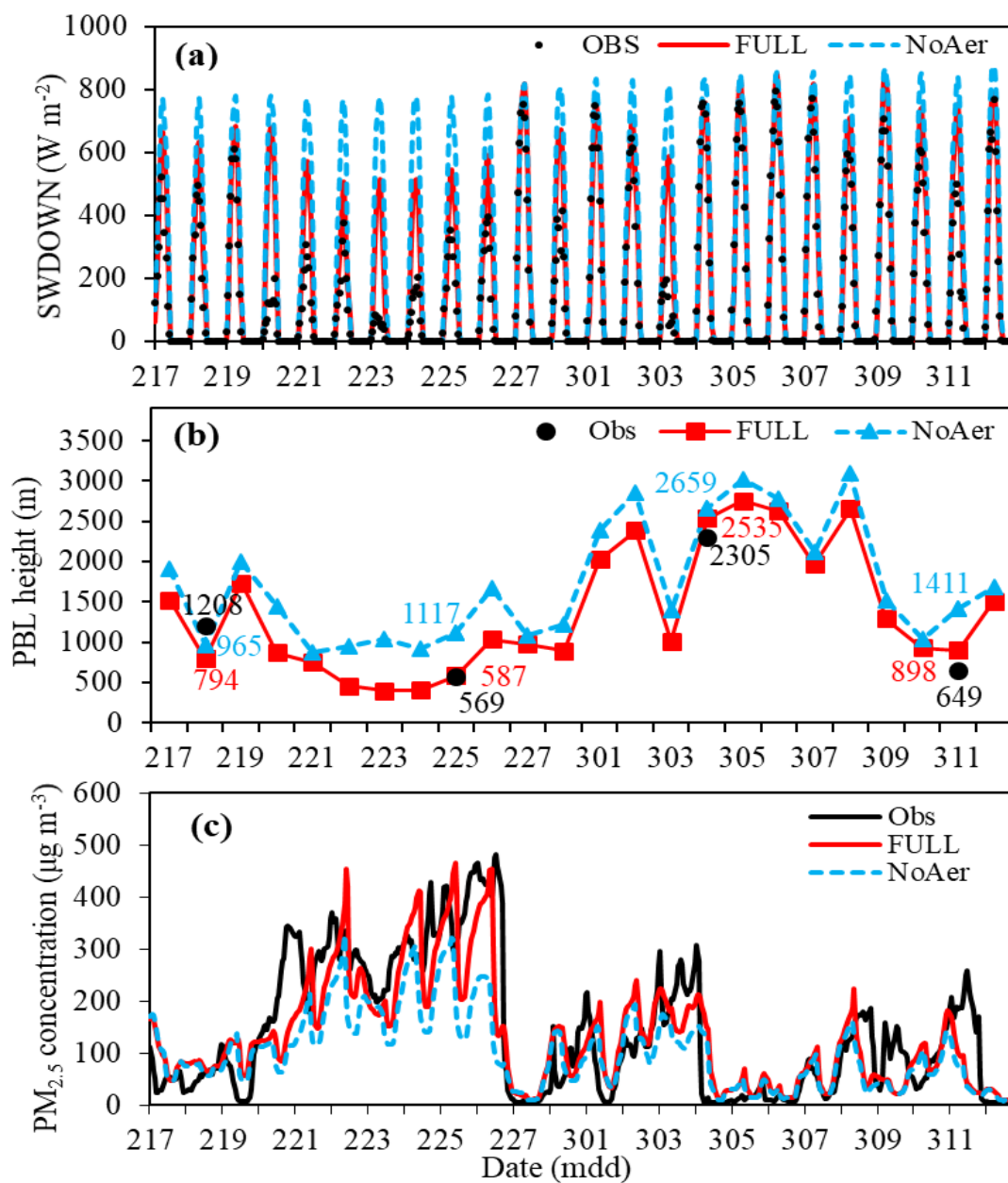
1705 Figure 2. The model simulated and observed (a) hourly SWDOWN at Xianghe, (b) hourly

1706 PBL height at 14:00 (LST) at Xianghe (note observations are available in the 4 days, numbers

1707 are observations and corresponding simulations) and (c) hourly $PM_{2.5}$ concentration at IAP in

1708 Beijing.

1709
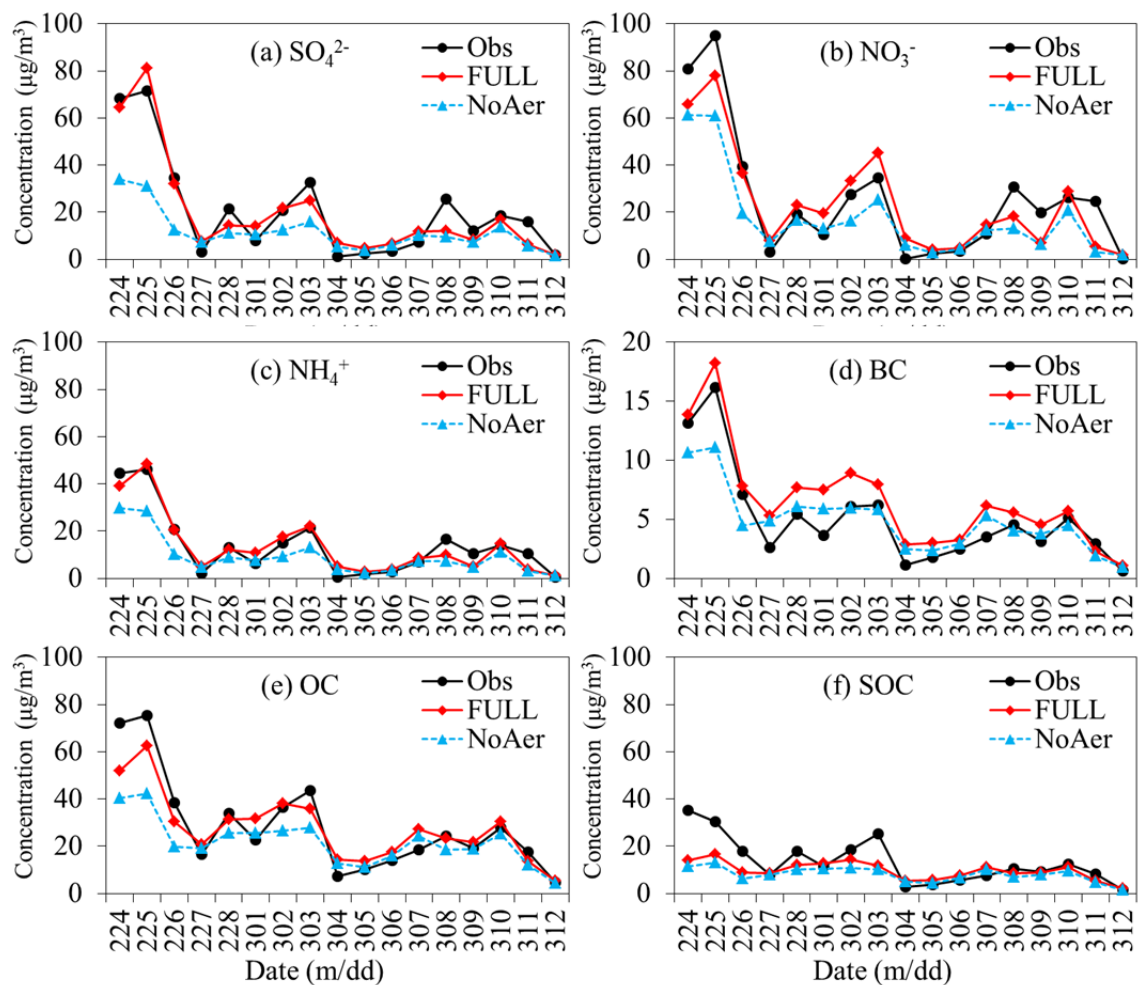
1710 Figure 3. The model simulated and observed daily mean concentrations of aerosol

1711 compositions in PM$_{2.5}$ at the IAP site in Beijing.

1712
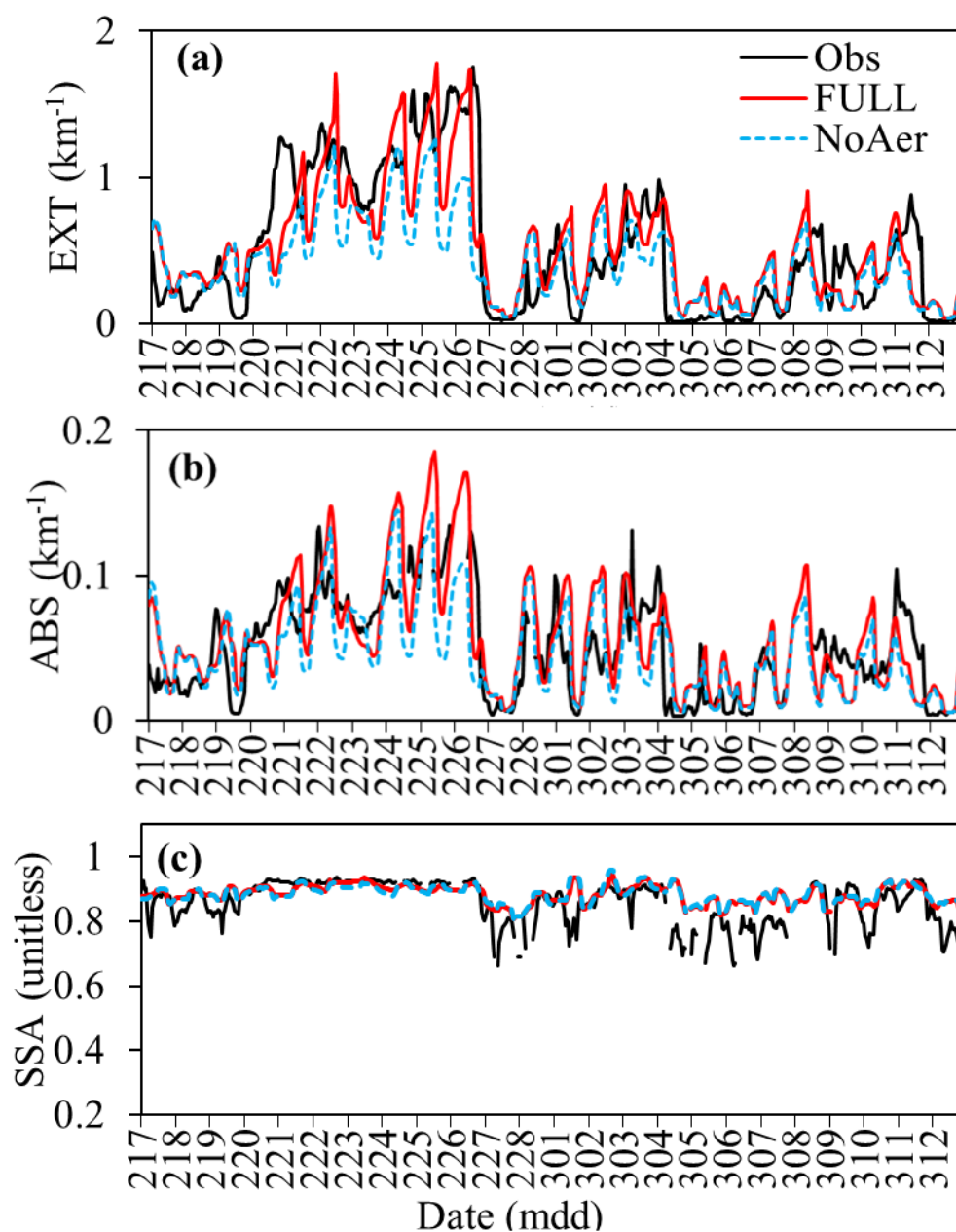
1713 Figure 4. The model simulated and observed hourly (a) aerosol extinction coefficient (EXT),

1714 (b) absorption coefficient (ABS) and (c) single scattering albedo (SSA) at the IAP site in

1715 Beijing under dry condition (RH=10%).
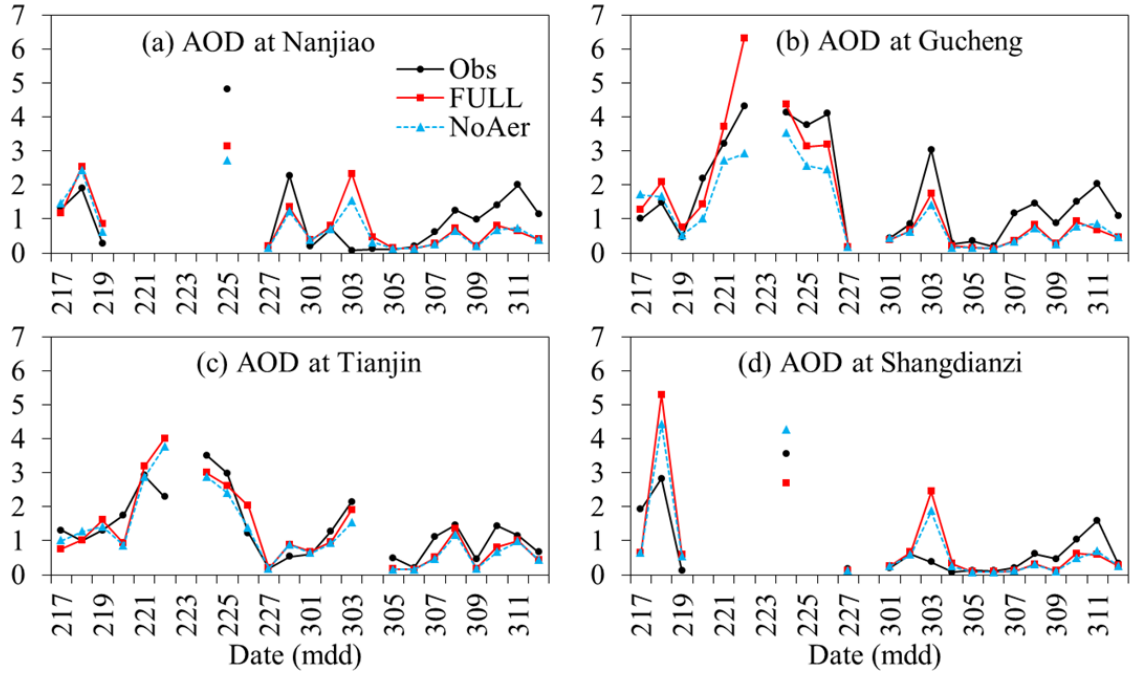
Figure 5. The model simulated and observed daily mean AOD (at 550 nm) at the four sites of CARSNET.
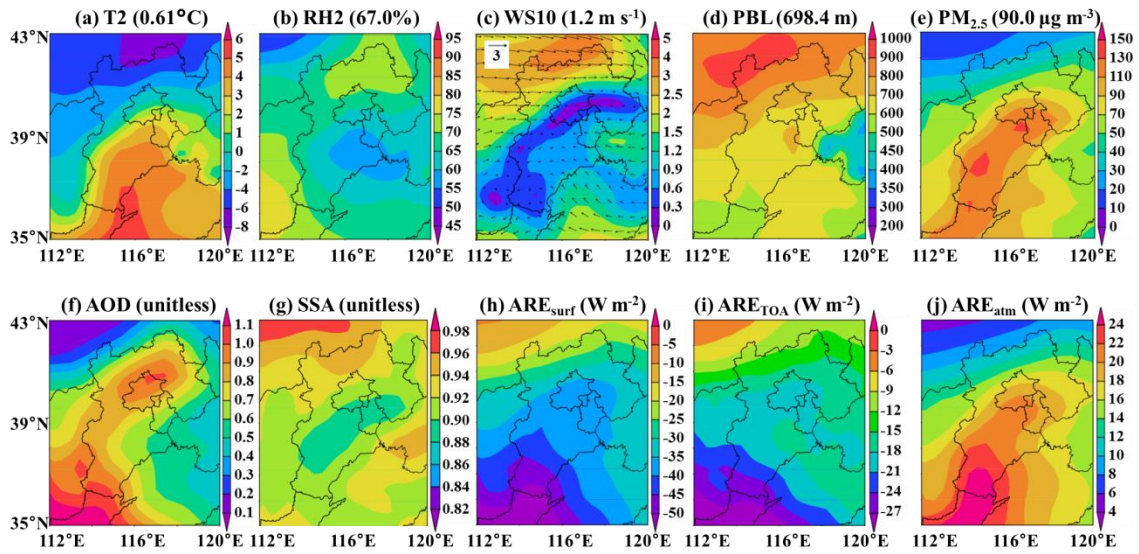
Figure 6. The model simulated (a) air temperature (T2), (b) relative humidity (RH2), (c) wind speed (WS10), (d) PBL height, (e) PM$_{2.5}$ concentration, (f) AOD, (g) SSA, (h) all-sky ARE at the surface, (i) all-sky ARE at the top of atmosphere and (j) all-sky ARE in the atmosphere from the FULL case. Numbers in the parentheses are averages over the BTH region during the entire study period.
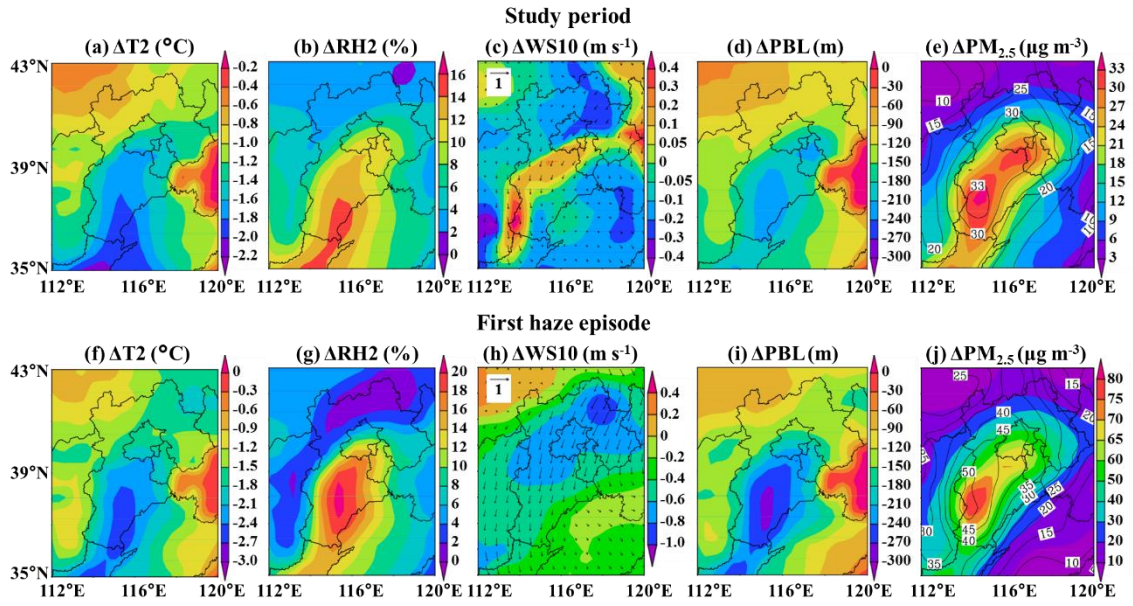
Figure 7. The model simulated feedback-induced changes (FULL minus NoAer) in (a, f) air temperature (T2), (b, g) relative humidity (RH2), (c, h) wind speed (WS10), (d, i) PBL height and (e, j) $PM_{2.5}$ concentration averaged over the entire study period (a-e) and over the first haze episode (20–26 February) (f-j). Units are given in the parentheses.
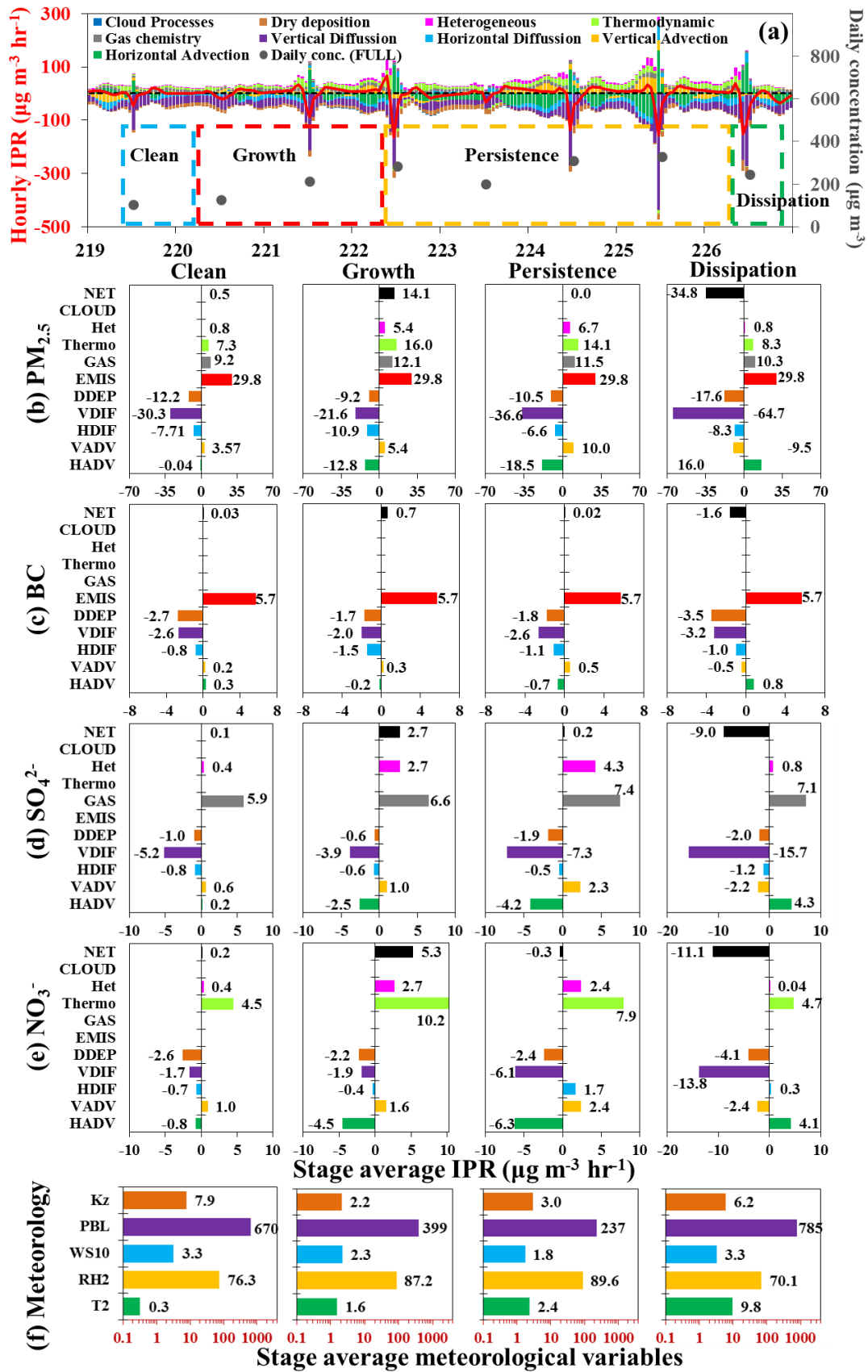
Figure 8. The model calculated integrated process rates (IPR) for the first haze episode (20–26 February) in Beijing. (a) hourly IPR, daily PM$_{2.5}$ concentration and the division of the four stages. The constant IPRs of emissions are not shown for clarity. The mean IPRs for (b) PM$_{2.5}$, (c) BC, (d) sulfate (SO$_4^{2-}$), nitrate (NO$_3^-$), and (f) mean meteorological variables in the four stages. Note that zero IPR values are not listed. Units of T2, RH2, WS10, PBL and K$_z$ are °C, %, m s^{-1}, m and m^2 s^{-1}, respectively.
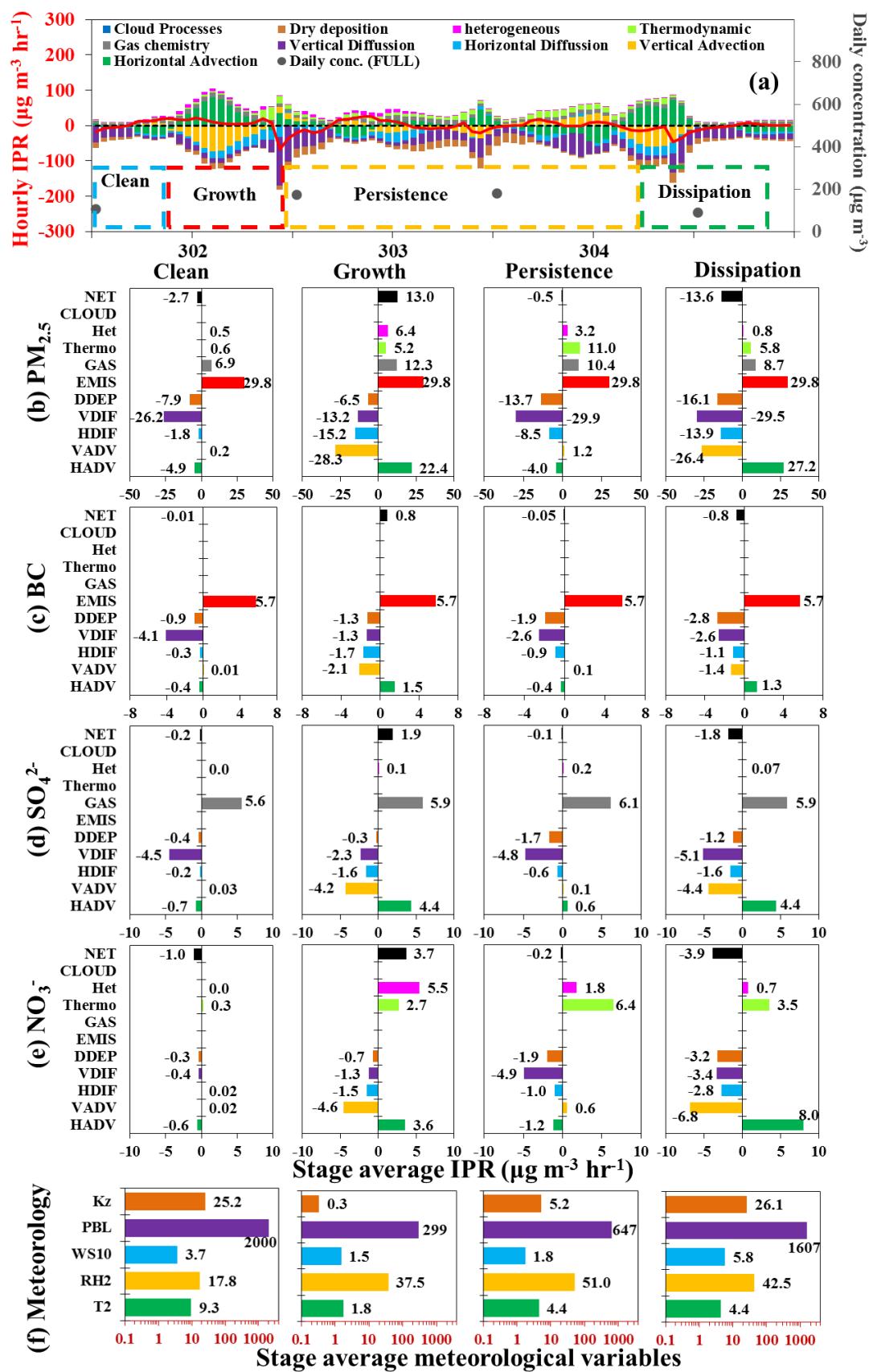
Figure 9. Same as Figure 8 but for the second haze episode (1–4 March).
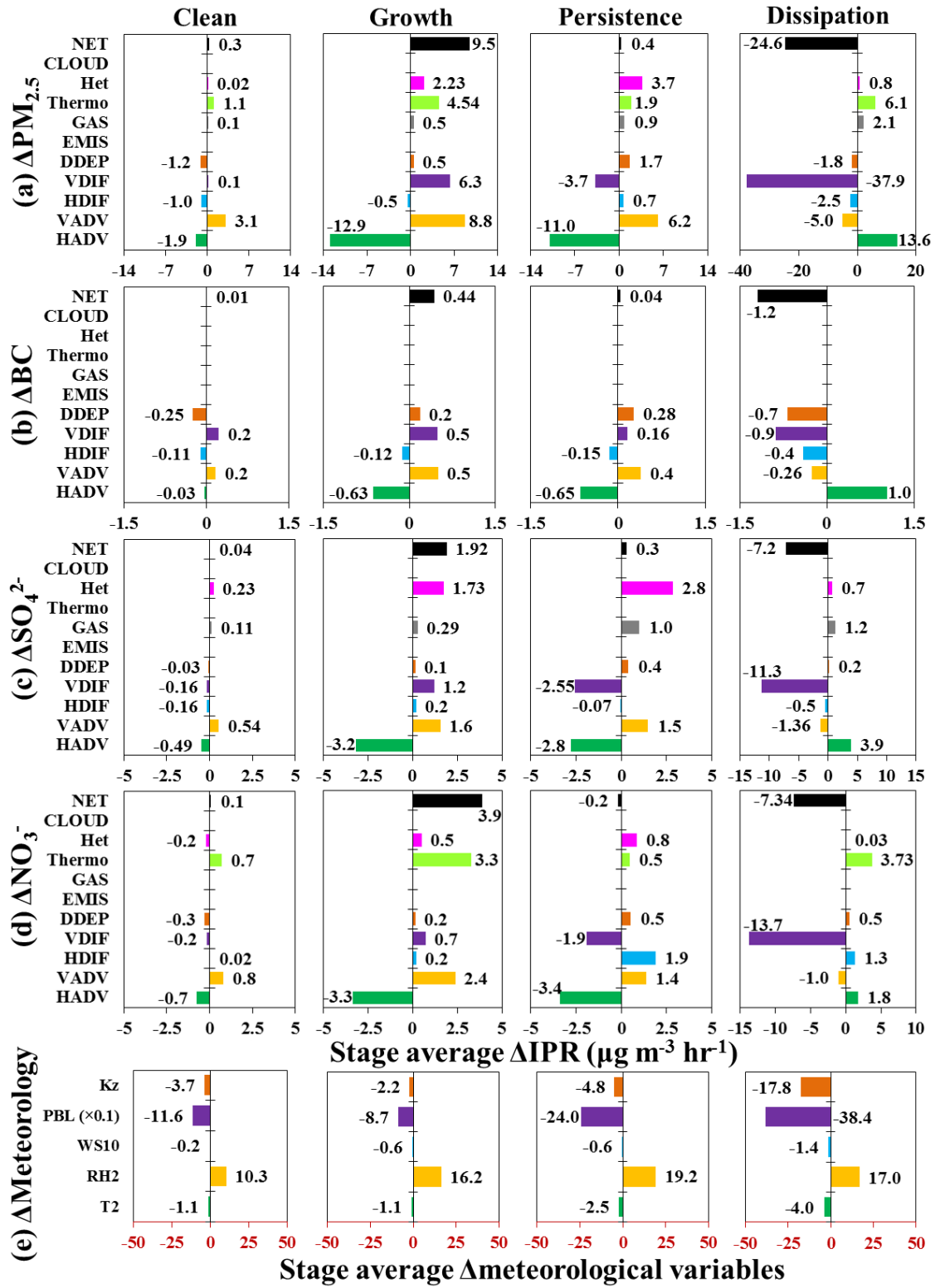
Figure 10. The feedback-induced mean changes in IPRs (FULL minus NoAer) for PM$_{2.5}$ and its chemical components and meteorological variables during the first haze episode (20–26 February) in Beijing. ΔIPRs for PM$_{2.5}$ and its chemical components and Δmeteorological variables are averages over the four stages. Note that zero ΔIPR values (no change) are not shown and the ΔPBL heights are scaled by 0.1. The division of the four stages and units are the same as those in Figure 8.
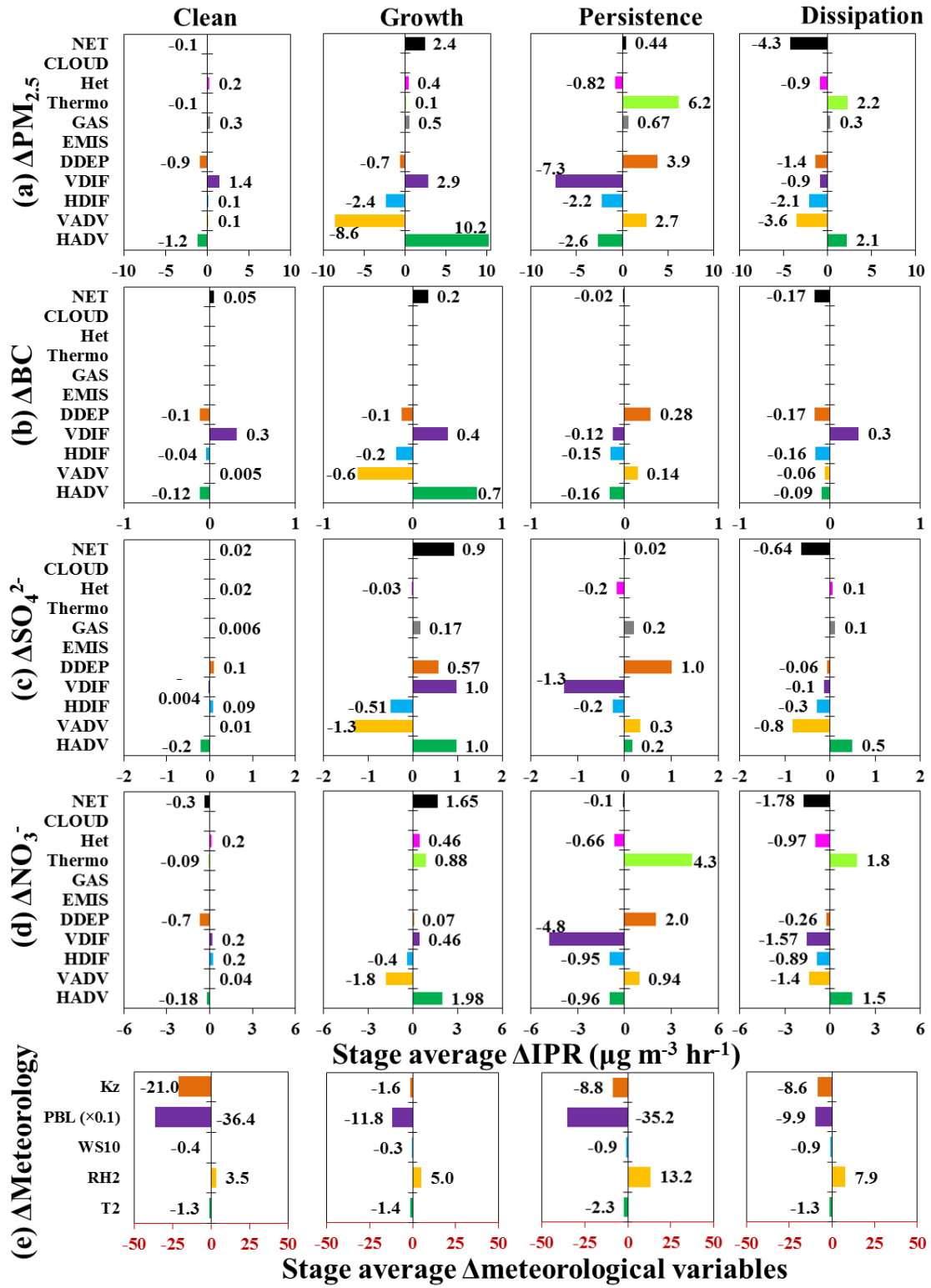
Figure 11. Same as Figure 10 but for the second haze episode (1–4 March). The division of the four stages are the same as that in Figure 9.

Table 1. Performance statistics for meteorological variables at observation sites in the BTH region. Mean observation (Obs), mean simulation (Sim), correlation coefficient (R) and normalized mean bias (NMB in %) are given. WS10, T2 and RH2 are wind speed at 10 meter, air temperature at 2 meter and relative humidity at 2 meter, respectively. All the sample numbers are 207.

Sites	Longitude	Latitude	WS10 (m s^{-1})				T2 (°C)				RH2 (%)				SWDOWN (W m^{-2})			
			Obs	Sim	R	NMB	Obs	Sim	R	NMB	Obs	Sim	R	NMB	Obs	Sim	R	NMB
FULL																		
Beijing	39°48'N	116°30'E	2.3	2.9	0.53	28%	3.0	2.5	0.77	-16%	53.4	62.6	0.72	17%				
Tianjin	39°6'N	117°6'E	2.6	3.1	0.53	23%	3.5	3.8	0.89	8%	62.9	59.2	0.68	-6%				
Tanggu	39°6'N	117°42'E	2.4	3.4	0.36	42%	3.0	3.1	0.84	2%	69.3	61.3	0.49	-12%				
Total			2.4	3.1	0.47	31%	3.2	3.1	0.83	-2%	61.9	61.0	0.61	-1%				
Xianghe	39°45'N	116°58'E													136.0	188.4	0.91	38%
NoAer																		
Beijing	39°48'N	116°30'E	2.3	3.4	0.48	48%	3.0	4.1	0.74	37%	53.4	51.1	0.68	-4%				
Tianjin	39°6'N	117°6'E	2.6	3.6	0.48	39%	3.5	5.3	0.88	51%	62.9	47.8	0.65	-24%				
Tanggu	39°6'N	117°42'E	2.4	3.8	0.28	60%	3.0	4.5	0.84	50%	69.3	51.4	0.48	-26%				
Total			2.4	3.6	0.41	49%	3.2	4.6	0.82	46%	61.9	50.1	0.59	-19%				
Xianghe	39°45'N	116°58'E													136.0	234.0	0.85	72%

Table 2. Performance statistics for PM$_{2.5}$ concentration and its chemical components, aerosol optical parameters at RH=10% (EXT, ABS and SSA) at the IAP site in Beijing. Mean observation (Obs), mean simulation (Sim), correlation coefficient (R) and normalized mean bias (NMB in %) are listed.

Species (unit)	Samples	Obs	FULL			NoAer		
			Sim	R	NMB	Sim	R	NMB
PM$_{2.5}$ (μg m^{-3})	570	142.0	131.4	0.80	-7%	101.2	0.73	-29%
SO$_4^{2-}$ (μg m^{-3})	33	21.0	20.3	0.92	-4%	11.9	0.88	-44%
NO$_3^-$ (μg m^{-3})	33	26.0	24.3	0.88	-6%	17.6	0.87	-32%
NH$_4^+$ (μg m^{-3})	33	14.1	13.9	0.91	-2%	9.4	0.89	-34%
BC (μg m^{-3})	33	5.2	6.7	0.92	28%	5.0	0.84	-3%
OC (μg m^{-3})	33	29.1	28.3	0.88	-3%	22.3	0.78	-24%
POC (μg m^{-3})	33	15.5	18.4	0.93	19%	14.1	0.87	-9%
SOC (μg m^{-3})	33	13.6	9.9	0.56	-27%	8.2	0.45	-40%
EXT (km^{-1})	570	0.51	0.53	0.79	4%	0.41	0.72	-19%
ABS (km^{-1})	534	0.048	0.052	0.68	10%	0.043	0.59	-11%
SSA (unitless)	534	0.85	0.88	0.65	5%	0.88	0.59	5%

Table 3. Performance statistics for daily mean AOD at the four CARSNET sites in the BTH region. Mean observation (Obs), mean simulation (Sim), correlation coefficient (R) and normalized mean bias (NMB, in the unit of %) are listed.

| | Samples | Obs | FULL | | | NoAer | | |
			Sim	R	NMB	Sim	R	NMB
Nanjiao	18	1.09	0.92	0.67	-15.6%	0.82	0.74	-24.9%
Gucheng	22	1.73	1.51	0.90	-12.8%	1.16	0.91	-33.0%
Tianjin	22	1.37	1.29	0.86	-5.7%	1.19	0.86	-12.8%
Shangdianzi	17	0.84	0.90	0.72	6.2%	0.89	0.85	5.0%
Total	79	1.29	1.18	0.81	-8.6%	1.03	0.82	-20.2%

Table 4. The model simulated domain and period averages of AOD, SSA and AREs from the FULL case over the BTH region.

	AOD (unitless)	SSA (unitless)	ARE_{surf} (W m^{-2})	ARE_{TOA} (W m^{-2})	ARE_{atm} (W m^{-2})
	Study period (17 February to 12 March)				
All day	0.78	0.91	-37	-18	19
Daytime	1.53	0.92	-79	-39	40
	First haze episode (20–26 February)				
All day	1.59	0.93	-57	-32	25
Daytime	3.17	0.93	-123	-69	53

3 Table 5. The model simulated feedback-induced changes (FULL minus NoAer) in T2, WS10, RH2, PBL

4 height, PM$_{2.5}$ concentration and vertical diffusion coefficient (K$_z$) averaged over the BTH region during the

5 entire period and the first haze episode. Inside the parentheses are percentage changes relative to the NoAer

6 case.

	ΔT2 (°C)	ΔWS10 (m s^{-1})	ΔRH2 (%)	ΔPBL height (m)	ΔPM$_{2.5}$ (μg m^{-3})	ΔK$_z$ (m^2 s^{-1})
			Study period (17 February to 12 March)			
All day	-1.4 (-69.4%)	-0.038 (-3.1%)	+8.7 (+14.9%)	-160.0 (-18.6%)	+20.0 (+28.6%)	-3.3 (-27.0%)
Daytime	-1.8 (-42.1%)	+0.028 (+1.9%)	+9.0 (+16.9%)	-267.1 (-22.4%)	+21.1 (+35.6%)	-6.7 (-27.6%)
			First haze episode (20–26 February)			
All day	-1.8 (-59.7%)	-0.52 (-19.5%)	+9.8 (+12.4%)	-183.6 (-31.0%)	+45.1 (+38.7%)	-3.9 (-48.8%)
Daytime	-2.5 (-46.6%)	-0.59 (-19.8%)	+10.4 (+13.8%)	-307.3 (-37.6%)	+49.3 (+48.5%)	-8.3 (-51.9%)

12 Table 6. Same as Table 5 but for Beijing.

	ΔT2 (°C)	ΔWS10 (m s^{-1})	ΔRH2 (%)	ΔPBLH (m)	ΔPM$_{2.5}$ (μg m^{-3})	ΔK$_z$ (m^2 s^{-1})
			Study period (17 February to 12 March)			
All day	-1.6 (-39.1%)	-0.48 (-13.9%)	+11.8 (+23.3%)	-154.0 (-18.3%)	+30.1 (+29.8%)	-4.5 (-37.5%)
Daytime	-2.3 (-33.1%)	-0.52 (-13.9%)	+12.5 (+28.1%)	-282.7 (-22.5%)	+34.0 (+43.9%)	-9.6 (-38.8%)
			First haze episode (20–26 February)			
All day	-2.1 (-46.1%)	-0.58 (-20.4%)	+17.0 (+24.5%)	-195.6 (-35.9%)	+68.0 (+39.1%)	-5.0 (-59.5%)
Daytime	-3.4 (-44.6%)	-0.78 (-23.9%)	+17.9 (+27.2%)	-358.3 (-45.5%)	+83.2 (+59.6%)	-11.0 (-63.2%)

22 Table 7. The model simulated feedback-induced changes (FULL minus NoAer) in BC, sulfate (SO_4^{2-}) and

23 nitrate (NO_3^-) averaged over the BTH region and Beijing during the entire period and the first haze episode.

24 Inside the parentheses are percentage changes relative to the NoAer case.

	Beijing-Tianjin-Hebei region (BTH)			Beijing		
	ΔBC ($\mu g\ m^{-3}$)	ΔSO_4^{2-} ($\mu g\ m^{-3}$)	ΔNO_3^- ($\mu g\ m^{-3}$)	ΔBC ($\mu g\ m^{-3}$)	ΔSO_4^{2-} ($\mu g\ m^{-3}$)	ΔNO_3^- ($\mu g\ m^{-3}$)
	Study period (17 February to 12 March)					
All day	+0.9 (+25.1%)	+5.0 (+46.4%)	+6.8 (+37.3%)	+1.6 (+27.5%)	+8.4 (+58.5%)	+8.4 (+36.9%)
Daytime	+1.0 (+39.5%)	+5.4 (+60.2%)	+7.2 (+43.2%)	+1.9 (+51.5%)	+9.5 (+86.5%)	+9.5 (+48.8%)
	First haze episode (20–26 February)					
All day	+1.9 (+32.9%)	+12.6 (+66.9%)	+14.6 (+40.9%)	+3.1 (+33.6%)	+22.3 (+81.8%)	+16.7 (+34.7%)
Daytime	+2.2 (+50.1%)	+13.8 (+81.4%)	+15.8 (+48.3%)	+4.1 (+62.3%)	+26.0 (+112.4%)	+20.9 (+51.5%)